Copyright

by

Eric Ou

2020

The Dissertation Committee for Eric Ou Certifies that this is the approved version of the following Dissertation:

Four-Probe Thermal Transport Measurements of Few-Layer Graphene and Ultrathin Graphite

Committee:

Li Shi, Supervisor

Matthew J. Hall

Emanuel Tutuc

Yaguo Wang

Four-Probe Thermal Transport Measurements of Few-Layer Graphene and Ultrathin Graphite

by

Eric Ou

Dissertation

Presented to the Faculty of the Graduate School of

The University of Texas at Austin

in Partial Fulfillment

of the Requirements

for the Degree of

Doctor of Philosophy

The University of Texas at Austin

August 2020

For mom and dad

Acknowledgements

Out of all the pieces of information that have managed to enter my brain during my post-secondary education, two bits have really stuck with me. The first was from a speech given by Ernest Cockrell, whose father is the namesake of the Cockrell School of Engineering as well as countless scholarships and endowed professorships. He said that when you see a turtle on a fence post, you know it didn't get there by itself. He expanded by stating that each one of us in that room, at that moment, only ended up there through the help of countless people along the way. As absurd as it is to liken scholarship recipients to stranded turtles stuck on fence posts, his analogy has reminded me to be thankful for and show gratitude to those who have helped me throughout my life. To those people, I hope that I have expressed this gratitude more personally than a single line in an acknowledgements section ever could.

The second thing that resonated with me, which the only people who end up reading this might find useful, is from someone whom I greatly respect recalling her experience during a qualification training program. When asked about overcoming obstacles, she said that every time she had difficulties, she would recall the moment when she first deeply desired to become a trainee in the program and since she made that decision sincerely, she decided that she should do her best to the end. Although I wish I could have finished my degree as earnestly as I started it, this mindset has given me strength in seriously difficult times and for that I am eternally grateful.

ABSTRACT

Four-Probe Thermal Transport Measurements of Few-Layer Graphene and Ultrathin Graphite

Eric Ou, Ph.D.

The University of Texas at Austin, 2020

Supervisor: Li Shi

The unique combination of mechanical, electrical, and thermal properties of graphite and its derivatives, such as graphene and carbon nanotubes, make graphitic materials desirable for a number of technological applications as well as a platform for studying various transport phenomena, especially at the nanoscale. Although it has been more than a decade since graphene was first successfully isolated, discrepancies between the results of theoretical and experimental studies have not yet been resolved and the answers to many fundamental questions concerning the details of thermal transport in graphene are still subject to debate. The presence of unknown contact thermal resistance has limited prior two-probe thermal transport measurements of suspended graphene samples. This work utilizes a four-probe thermal measurement technique to measure few-layer graphene and ultrathin graphite samples. This technique has the ability to measure the intrinsic thermal conductance of suspended samples and to isolate the contact thermal resistance between the sample and measurement device. By eliminating error due to contact thermal resistance and developing a clean method for transferring thin-film

samples, the true intrinsic thermal properties of graphene can be realized, potentially leading to the observation of unique transport phenomena such as hydrodynamic phonon transport.

Table of Contents

List of Figures x

Chapter 1: Introduction 1

1.1 Background 1

1.2 Scope of Work 4

Chapter 2: Suspended Micro-device Thermometry of Few-layer Graphene Using the Four-Probe Thermal Measurement Method 6

2.1 Introduction 6

2.2 Experimental Method 6

2.2.1 Thermal Conductance Measurement Using a Four-Probe Method 6

2.2.2 Considerations When Using the Four-Probe Thermal Measurement Technique 12

2.2.3 Four-Probe Thermal Measurement Micro-Thermometry Device Fabrication 16

2.2.4 Sample Preparation 19

2.2.5 Sample Characterization 22

2.3 Results and Discussion 24

2.3 Conclusion 27

Chapter 3: Suspended Micro-device Thermometry of Ultrathin Graphite Using Four-Probe Thermal Measurement Method and a Hard Mask Shielded Transfer Technique 29

3.1 Introduction 29

3.2 Experimental Method 30

3.2.1. Sample Preparation 30

3.2.2 Multi-Probe Thermal Measurement Method 34

3.3 Results and Discussion 36

3.4 Conclusion 44

Chapter 4: Fabrication of a Fully Supported Four-Probe Thermal Measurement Device Using a Vertically Embedded Sacrificial Oxide for Clean Transfer of Graphene Samples 45

4.1 Introduction...45

4.2 Device Fabrication and Sample Assembly 45

4.2.1 Introduction...45

4.2.2 Method..47

4.2.3 Challenges...52

4.3 Conclusion 53

Chapter 5: Conclusion...54

Bibliography 56

List of Figures

Figure 2.1: (a) Optical and (b) scanning electron micrographs of a 3.8 μm wide, 7-layer thick patterned FLG sample assembled across four suspended Pd/SiN_x beams, each of which acts as a resistance thermometer (RT). Additional Pd pads were deposited on top of the FLG sample to clamp the graphene sample onto the thermometer lines. (c) Thermal resistance circuit of the measurement device when the first thermometer line is Joule heated with power $(IV)_1$. $R_{b,j}$ is the thermal resistance of the jth RT beam. $R_{c,j}$ represents the thermal contact resistance between the sample and the jth RT. R_1, R_2, and R_3 represent the intrinsic thermal resistances of the three suspended sample segments. $\theta_{c,j,i}$ is the jth RT temperature rise at the contact point with the sample when the ith line is heated. θ_0 is the temperature rise at the point where the suspended RT lines terminate into the bulk substrate. $Q_{j,i}$ is the heat flow from the jth line to the sample when the ith line is heated. 8

Figure 2.2: (a) Measured electrical resistance change of the thermometer lines as a function of the heating current through the first thermometer line. (b) Measured electrical resistances of the four thermometer lines at a low bias current as a function of the stage temperature. 11

Figure 2.3: (a) Optical micrograph of a 15 μm wide exfoliated graphite ribbon on a four-probe thermal measurement device. (b) Contact point temperature, $\theta_{c,j}$, as a function of the heating current through the first thermometer line. The mismatch between the sample thermal resistance and the device beam thermal resistance results in extremely small contact point temperature differences between thermometer lines. 13

Figure 2.4: Measured thermal resistances of the sample and the average thermal resistance of the thermometer lines. The random uncertainty of the values does not exceed marker size. 15
Figure 2.5: Procedure for placing a sample on the measurement device with a polymer carrier layer....................21
Figure 2.6: Atomic force microscope scan of the 7-layer graphene sample before patterning. The thickness of the sample was determined by averaging the step height measured at multiple points on the right edge of the scan. 22
Figure 2.7: Raman spectrum of the middle-suspended segment of the sample. 23
Figure 2.8: Measured and calculated thermal conductivity as a function of temperature. Shown for comparison is the highest basal-plane thermal conductivity reported for bulk graphite included in Touloukian et al. The relaxation time is obtained from a simple scattering model using the specific heat and group velocity calculated from the phonon dispersion of 7-layer graphene and fitting the experimental data. The relaxation time is found to increase with increasing phonon frequency as τ-1 ∝ ωα, where α is 0.162, 0.135, and 0.137 for the As Transferred, 1 Hour Anneal, and 9 Hour Anneal measurements respectively. The increasing τ^{-1} with phonon frequency indicates that the intrinsic phonon-phonon scattering is not negligible compared to the extrinsic scattering by polymeric residue....................26

Figure 3.1: (a) Natural graphite flake exfoliated onto a silicon wafer with 300 nm thermally grown silicon oxide (b) Prefabricated oxide beam that has been transferred onto the exfoliated flake (c) Oxide beam and graphite flake after O_2 plasma etching. The oxide beam serves as a hard mask for the dry etching process. (d) Graphite flake and oxide beam that have been transferred together onto eight thermometer lines supported on a Si substrate using a PMMA transfer film. 32

Figure 3.2: (a) Optical micrograph of sample assembly procedure after all e-beam lithography steps. This representative sample is ready for metal deposition. (b) Optical micrography of the oxide beam after metal lift-off. The metal that has been selectively deposited helps to anchor the oxide beam when the PMMA transfer film is removed. 34

Figure 3.3: Thermal circuit for a sample assembled across a measurement device with eight suspended thermometer lines. The thermal resistance of each of the sample segments suspended between device lines are represented by $R_{s,n}$ for $n=1$ to 7. At each sample and device interface, there is some contact resistance between the sample and the jth line, $R_{c,j}$. Each device beam has some thermal resistance, $R_{b,j}$, for the jth beam. Each device beam is thermally grounded into the device substrate and maintains a temperature rise above sample stage temperature of $\theta_0=0$. $\theta_{c,j}$ is the temperature rise above sample stage temperature of the jth device line at the sample contact point. 36

Figure 3.4: (a) Optical and (b) scanning electron micrographs of a 7.71 nm thick sample that has been patterned into a 45 μm long and 3.7 μm wide ribbon and transferred across eight lines of the four-probe thermal measurement device. (c) Optical and scanning (d) electron micrograph of a 7.37 nm thick graphite sample transferred onto four lines of a four-probe measurement device. 37

Figure 3.5: Change in electrical resistance of the jth sensing line vs heating current in the 5th line for $j=4$ (a) and $j=6$ (b) of the 7.71 nm thick sample transferred across eight lines. The suspended sample segment between the 4th and 5th lines was damaged during measurement, resulting in no heat flow between those lines. 38

Figure 3.6: Measured thermal conductivity as a function of temperature for three suspended natural graphite samples of various thicknesses and lengths. 39

Figure 3.7: Optical micrograph of 7.04nm thick sample exfoliated from high oriented pyrolytic graphite patterned into an 18 μm long, 1.7 μm wide ribbon and transferred across four lines of a four-probe thermal measurement device. 41

Figure 3.8: Measured thermal conductivity as a function of temperature of the exfoliated highly oriented pyrolytic graphite (HOPG) sample compared to three exfoliated natural graphite (NG) samples. 41

Figure 3.9: Scale drawing of a sample that has been transferred onto a partially supported measurement device. All EBL steps have been performed and the assembly is ready for metal deposition. The supported device consists of the silicon substrate (gray), nitride beams (green) and contact metal (silver). The sample and oxide beam (purple) have been transferred onto the device using a PMMA carrier layer (blue), which has been patterned using EBL. The sample is attached to the bottom of the oxide beam and is not in direct contact with any polymer layers. 42

Figure 3.10: Raman spectrum of the middle-suspended segment of the 7.71 nm thick, 5 μm long sample. 43

Figure 4.1: Orthographic and top views of the fully supported four-probe thermal measurement device fabrication. (a) Silicon substrate (gray), with deposited silicon nitride (green), sputtered metal (silver), and sputtered silicon oxide (purple). (b) Silicon oxide hard mask is patterned using photolithography and dry etching. (c) Metal layers are patterned using the silicon oxide hard mask and dry etching. (d) Silicon nitride window is patterned using photolithography and dry etching. (e) Silicon oxide is sputter onto the wafers, acting as vertically embedded sacrificial oxide. (f) CMP of sacrificial oxide to create flat substrate. 50

Figure 4.2: Partial cross-section view of sacrificial oxide layer fabrication around the device lines of the four-probe thermal measurement device. (a) Silicon substrate (gray), with deposited silicon nitride (green), sputtered metal (silver), and sputtered silicon oxide (purple). (b) Silicon oxide hard mask is patterned using photolithography and dry etching. (c) Metal layers are patterned using the silicon oxide hard mask and dry etching. (d) Silicon nitride window is patterned using photolithography and dry etching (e) Silicon oxide is sputter onto the wafers, acting as vertically embedded sacrificial oxide. (f) CMP of sacrificial oxide to create flat substrate. 51

Figure 4.3: Optical image of a 4-inch silicon wafer with deposited silicon nitride and silicon oxide layers after the CMP process. The nitride and oxide layers at the edge of the wafer have been completely removed; the remaining nitride and oxide layers have varying thicknesses, creating color gradients radially from the center of the wafer. 53

Chapter 1: Introduction

1.1 Background

Due to its combination of excellent mechanical,[1] electrical,[2,3] and thermal properties,[4] graphene has garnered much attention not only for its potential for practical applications such as thermal management[5–7] and electronic devices,[8–10] but also for its suitability as a platform for studying various transport phenomena.[11–13] Although it has been more than a decade since the first report of successfully isolated graphene samples,[14] many discrepancies between the results of theoretical and experimental studies have not been resolved and the answers to many fundamental questions concerning the details of thermal transport in graphene are still subject to debate.

Graphitic materials are among the best-known thermal conductors; the basal plane thermal conductivity of graphite and its derivatives, including graphene and carbon nanotubes, rivals the record high value of diamond.[4,15] Although the high thermal conductivity of both diamond and graphitic materials can be generally described by Slack's high-thermal conductivity criteria based on the strongly bonded light elements,[16] there are intriguing unanswered questions on the microscopic mechanisms behind the distinct high thermal conductivity of graphitic materials.

One unusual feature in the vibration spectrum of graphitic materials is the presence of an out-of-plane bending or flexural modes for which the frequency increases quadratically with increasing wave vector. Compared to the in-plane polarized modes, these low-frequency flexural modes dominate the specific heat and make an important contribution to the high basal-plane thermal conductivity according to first principles calculations.[17]

Many factors, such as isotope concentration and size, have the potential to influence thermal transport. Both in-plane and out-of-plane phonon modes are influenced by isotope substitution; the increased mass disorder enhances phonon scattering which in turn reduces thermal conductivity. Recent first-principle calculations suggest that normal scattering processes dominate over non-momentum-conserving Umklapp phonon-phonon scattering processes in both suspended graphene and graphite, even near room temperatures.[18,19] Consequently, phonon transport in graphene and graphite can exhibit hydrodynamic transport features similar to molecular flows, including unique size and temperature dependencies that cannot be explained by diffusive transport described by the Fourier's law and ballistic phonon transport theory captured by the Landauer-Büttiker formalism.[19–21] The presence of these unusual non-diffusive, ballistic or hydrodynamic features in the intrinsic phonon transport process can have practical impact on the dependence of the apparent thermal conductivity of the graphitic materials on the size, shape, temperature, and interface interaction. Therefore, experimental investigation of these non-diffusive behaviors has become an area of intense research over the past two decades.

While there has been a surge of interest in nanoscale materials, characterization of thermal transport properties of these materials, especially 2D materials, has remained a challenging and often laborious task. The equipment required to fabricate the structures and devices used for measuring these samples combine with often complicated sample assembly has created a high barrier of entry for the field and impeded innovation. The techniques that have been used to measure the thermal properties of graphene, some more than a decade old, predominantly fall into two categories: optothermal techniques and electrothermal techniques.

The first thermal measurements of graphene were performed using a Raman-spectroscopy-based optothermal technique in which graphene is suspended over a trench or hole of known geometry and the sample is heated by the laser light, resulting in a local temperature rise and a corresponding frequency shift of the Raman G peak.[22] The G peak shift can be found as a function of sample temperature by using low laser excitation power to minimize local heating while externally heating or cooling the sample stage to manipulate the base sample temperature. While Raman optothermal methods are relatively simple to set up, the measured results vary considerably; the reported thermal conductivity of single layer graphene ranges from 600-5300 $Wm^{-1}K^{-1}$ near room temperature.[22–27] These measurements often have large uncertainties, sometimes larger than 50% of the reported value due to large variations in the reported optical absorption values of graphene. The temperature sensitivity of optothermal techniques is also limited due to the poor temperature sensitivity of the G peak shift; a relatively high amount of laser power is required to heat the sample enough so that the G peak shift can be observed, resulting in large temperature gradients between the heated area and substrate. Additionally, the tightly focused laser can cause complications due to strain and local non-equilibrium of phonons inside the laser spot.[28]

In addition to optothermal techniques, sensitive thermal transport measurement methods based on electro-thermo-microbridge devices have been used to observe the temperature and size dependence in the thermal conductivity of carbon nanotubes and graphene.[15,29,30] These devices require complicated fabrication procedures and precise sample alignment, but offer high temperature sensitivity and accurate heat flow measurement.[31–36] These devices typically rely on metal thermometer lines which exhibit a change in resistance based on temperature, the temperature coefficient of resistance, which can be calibrated at different externally controlled sample stage temperatures, the

same way as the Raman peak shift in the optothermal methods. When used to measure high conductance thin-film samples, these measurement devices can suffer from inaccurate temperature sensing for high conductance samples due to the positioning of the serpentine thermometers relative to the sample.[37]

An important limitation shared by both of the previously used optothermal and electro-thermo-microbridge methods, which have been used extensively in the micro- and nanoscale thermal measurement field, is the inability to separate the extrinsic thermal contact resistance from the intrinsic thermal resistance of the sample, which can be a major source of error for thin-film samples.[38] This limitation can complicate the interpretation of the experimental results and prevent the observation of phenomena such as non-diffusive phonon transport.

In summary, two main techniques, optothermal and electrothermal, have been utilized to measure the thermal properties of graphene and thin graphite samples; however, none of the currently utilized techniques have had the ability to eliminate contact thermal resistance, an important source of error for nanoscale materials.

1.2 Scope of Work

The aim of this work is to investigate the intrinsic thermal transport properties of graphene, and to search for features of hydrodynamic phonon transport. The specific objectives of the research include the development of a measurement methodology to minimize or eliminate common sources of error encountered in current micro-thermometry techniques and to use this methodology to experimentally determine the intrinsic thermal properties of graphene and ultrathin graphite. This dissertation consists of two experimental works and the framework for a third experimental work.

Chapter 2 reports the thermal conductivity measurements of few-layer graphene (FLG) using the four-probe thermal measurement method, which can isolate contact thermal resistance and measure the intrinsic thermal conductance of a suspended sample.[39] The high temperature of the peak thermal conductivity and overall low thermal conductivity of the sample compared to theoretical simulations and other experimental works suggest that polymer residue from the sample assembly process is suppressing the thermal conductivity of the sample, preventing the true intrinsic properties of graphene to be realized.

Chapter 3 reports modifications to the sample assembly process used in Chapter 2 in an attempt to reduce polymer contamination and measure the true intrinsic thermal properties of the graphene. In the modified sample assembly procedure, the samples are shielded from direct polymer contact through the use of a silicon oxide hard mask. Multiple ultrathin graphite samples were prepared using the new sample assembly process and measured using the four-probe thermal measurement technique. The reduced thermal conductivity of the exfoliated graphite samples compared to literature bulk values for the natural graphite source used for exfoliation suggests that polymer contamination through indirect contact may still be suppressing thermal performance.

Chapter 4 provides the framework for a sample assembly technique which will fully shield both sides of a thin-film sample during the majority of the sample assembly process onto a four-probe thermal measurement device, eliminating remaining sources of polymer contamination.

Chapter 5 summarizes the major findings from the experimental investigations presented in this dissertation and suggests additional experiments to address the challenge in measuring the intrinsic thermal transport properties of graphene.

Chapter 2: Suspended Micro-device Thermometry of Few-layer Graphene Using the Four-Probe Thermal Measurement Method[1]

2.1 Introduction

While the thermal properties of graphene have been extensively studied, an important limitation shared by many of the previously used optothermal and electro-thermo-microbridge methods is the inability to separate the extrinsic contact thermal resistance from the intrinsic thermal resistance of the sample. This limitation, which can be a major source of error, especially for thin-film samples, complicates the interpretation of the experimental results and prevents the observation of phenomena such as non-diffusive phonon transport.

This chapter reports results from temperature-dependent thermal conductivity measurements of suspended few-layer graphene (FLG) using a four-probe thermal measurement technique, which has the ability to separately measure the intrinsic thermal conductance of a sample and contact thermal resistance between the sample and measurement device.

2.2 Experimental Method

2.2.1 Thermal Conductance Measurement Using a Four-Probe Method

The four-probe thermal measurement technique, like the four-terminal electrical impedance measurement technique, uses multiple probes to measure the properties of a target measurement area. While at a high level, these measurement techniques are

[1] The content of this chapter was published in Ou, E., Li, X., Lee, S., Watanabe, K., Taniguchi, T., and Shi, L. "Four-Probe Measurement of Thermal Transport in Suspended Few-Layer Graphene With Polymer Residue." ASME. J. Heat Transfer. June 2019; 141(6): 061601. K.W. and T.T. provided the highly oriented pyrolytic graphite samples. E.O. fabricated the measurement devices, assembled the graphene sample, and performed measurements. X.L. and S.L. performed the thermal conductivity calculations. E.O. and L.S. wrote the manuscript and all other authors commented on and edited the manuscript.

similar, due to the nature of heat transfer and limitations in nano- and micro-scale fabrication, the four-probe thermal measurement technique is much more complicated to use than the electrical version. The thermal analogue of current, heat flow, is difficult to measure directly. Additionally, temperature is difficult to probe without parasitic heat loss. Due to these challenges, the device used for this measurement method does not attempt to measure heat flow directly or prevent heat loss through the temperature probes, unlike four-terminal electrical measurements where, in general, current can be measured directly and the high input impedance of the voltage probes minimizes current through the sensing leads to minimize voltage drop in the leads.

The device for this measurement method consists of four suspended beams composed of a nitride membrane that supports a layer of patterned thin-film metal lines which can act as both a resistance thermometer when low-bias currents are passed through as well as a Joule heater when large currents are supplied. Each metal line terminates into four contact pads, two on each side of the suspended segment, so that the four-probe electrical resistance of each suspended line can be monitored during the measurement. The sample is transferred onto the measurement device so that it bridges all four suspended beams as shown in Figure 2.1a. The measurement is performed under high vacuum in a temperature-controlled cryostat with multiple radiation shields to minimize convective and radiative heat transfer.

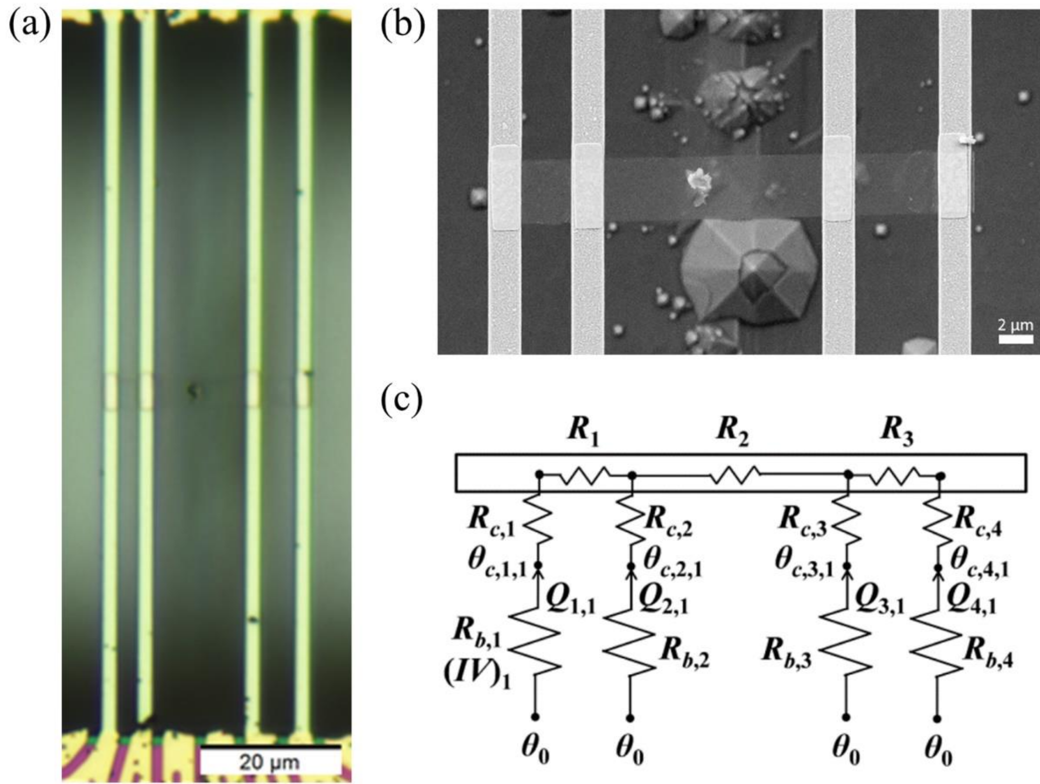

Figure 2.1: (a) Optical and (b) scanning electron micrographs of a 3.8 μm wide, 7-layer thick patterned FLG sample assembled across four suspended Pd/SiN_x beams, each of which acts as a resistance thermometer (RT). Additional Pd pads were deposited on top of the FLG sample to clamp the graphene sample onto the thermometer lines. (c) Thermal resistance circuit of the measurement device when the first thermometer line is Joule heated with power $(IV)_1$. $R_{b,j}$ is the thermal resistance of the jth RT beam. $R_{c,j}$ represents the thermal contact resistance between the sample and the jth RT. R_1, R_2, and R_3 represent the intrinsic thermal resistances of the three suspended sample segments. $\theta_{c,j,i}$ is the jth RT temperature rise at the contact point with the sample when the ith line is heated. θ_0 is the temperature rise at the point where the suspended RT lines terminate into the bulk substrate. $Q_{j,i}$ is the heat flow from the jth line to the sample when the ith line is heated.

This system can be represented as a thermal circuit shown in Figure 2.1c after making some simplifying assumptions. First, the area at the ends of the suspended beams, which is fully supported by the silicon substrate, is assumed to have low enough thermal spreading resistance so that it acts as a perfect heat sink and keeps the temperature rise at the ends of the lines at $\theta_0 = 0$ K, the same as the base substrate and cryostat stage temperature. Second, the suspended beams are designed to have a large aspect ratio so that heat transfer at steady state can be assumed to be one-dimensional along the length of each beam. Similarly, the samples are patterned into a ribbon shape and heat transfer along the sample is also assumed to be one-dimensional along length of the sample, which is perpendicular to the length of the suspended beams. Last, the area of the suspended beam where the sample contacts the beam is assumed to be at a uniform temperature, $\theta_{c,j,i}$, where j denotes the sensing line and i denotes the heated line.[40] The metal tags used for sample alignment helps with the temperature uniformity. This assumption greatly simplifies the data analysis since the point contact temperature must be calculated using the average temperature rise found from the average resistance change of the line and the temperature profile along the length of the line found by solving the heat conduction equation.

The four-probe thermal measurement is performed by resistively heating a single thermometer line while simultaneously measuring the resistances of all thermometer lines as seen in Figure 2.2a. This process is repeated until each line has been electrically heated. By measuring the resistance of the thermometer lines at different temperatures with a low bias current, shown in Figure 2.2b, we obtain the temperature coefficient of resistance and use it to convert the measured change in electrical resistance to the average temperature rise in each thermometer line when Joule heating is applied to the heater line. Based on the parabolic and linear temperature profiles for the heating line and the

thermometer lines, respectively, the contact point temperature rise between line j and the sample for heated line i with a Joule heating rate $(IV)_i$, $\theta_{c,j,i}$, can be obtained. The sixteen $\theta_{c,j,i}/(IV)_i$ data with both i and j ranging from 1 to 4 can allow us to obtain the thermal resistance of the four thermometer lines, $R_{b,j}$, the intrinsic thermal resistance of the sample (R_2) and the contact resistances ($R_{c,2}$ and $R_{c,3}$) between the sample and thermometer lines 2 and 3, as well as the combined intrinsic and contact thermal resistance, $R_1 + R_{c,1}$ and $R_3 + R_{c,4}$, of the two end segments of the sample. Here, R_2 can be separated from $R_{c,2}$ and $R_{c,3}$ because the heat flow through the middle sample segment differs from that through each of the two middle contacts. In comparison, the heat flow through an end segment is the same as that through the corresponding end contact, so that the intrinsic thermal resistance of the end segment cannot be separated from the end contact thermal resistance. Additional details of the four-probe thermal measurement technique can be found elsewhere.[39]

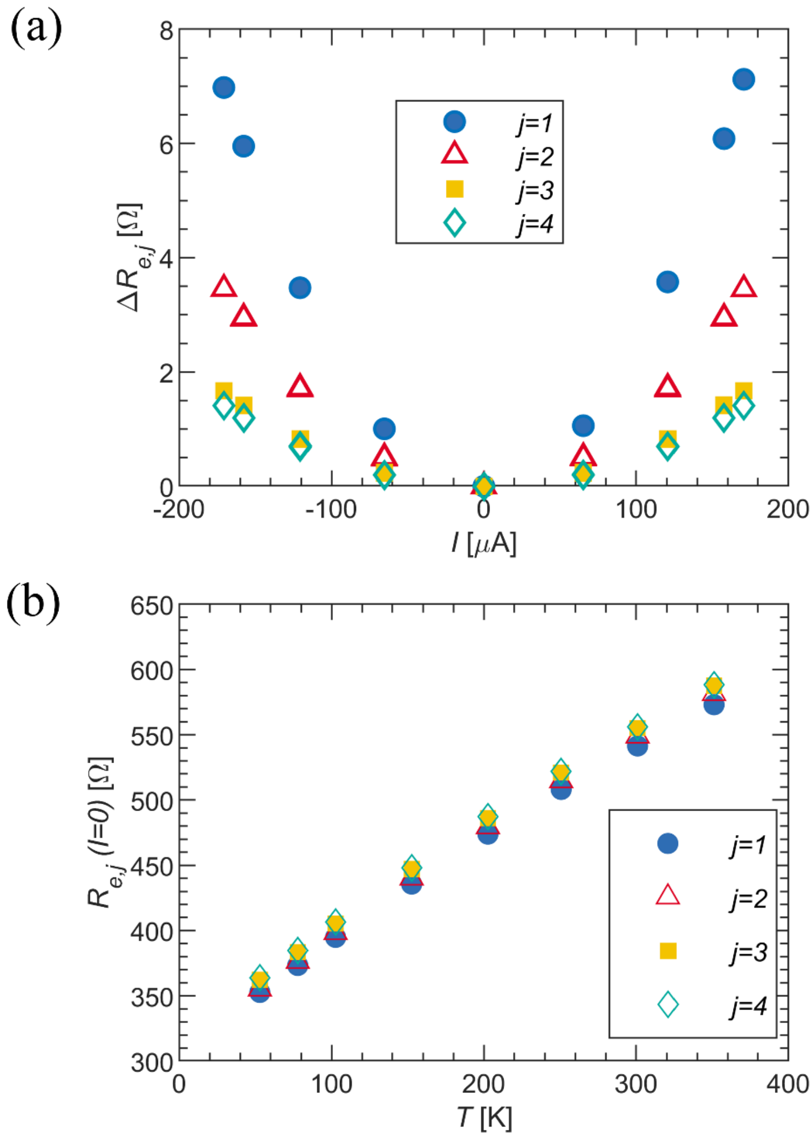

Figure 2.2: (a) Measured electrical resistance change of the thermometer lines as a function of the heating current through the first thermometer line. (b) Measured electrical resistances of the four thermometer lines at a low bias current as a function of the stage temperature.

2.2.2 Considerations When Using the Four-Probe Thermal Measurement Technique

To ensure a measurable signal when using the four-probe thermal measurement technique, the thermal resistance of the device beams should be tuned to match the sample thermal resistance. Without the thermal resistance matching, it is possible for the thermal signal of the sample to be too small to be measured or the temperature difference between the adjacent thermometer lines to be too small to be differentiated. If the thermal resistance of the sample is much higher than the device beam thermal resistance, heat flow to the other resistance thermometer lines through the sample is impeded and the majority of the heat will flow from the heated beam into the substrate which acts as a thermal ground or heat sink. Conversely, if the sample thermal resistance is much lower than the device beam resistance, the device lines will be thermally shorted by the sample, resulting in extremely small differences between the contact point temperatures. The sample shown in Figure 2.3a, which was transferred directly to the measurement device using a sharp tungsten probe mounted on a micro-manipulator stage, has a sample resistance R_2 approximately two orders of magnitude lower than the beam resistance R_b, and as a result the temperature rise of each line, $\theta_{c,i}$, shown in Figure 2.3b are nearly identical, making it difficult to calculate the heat flows accurately.

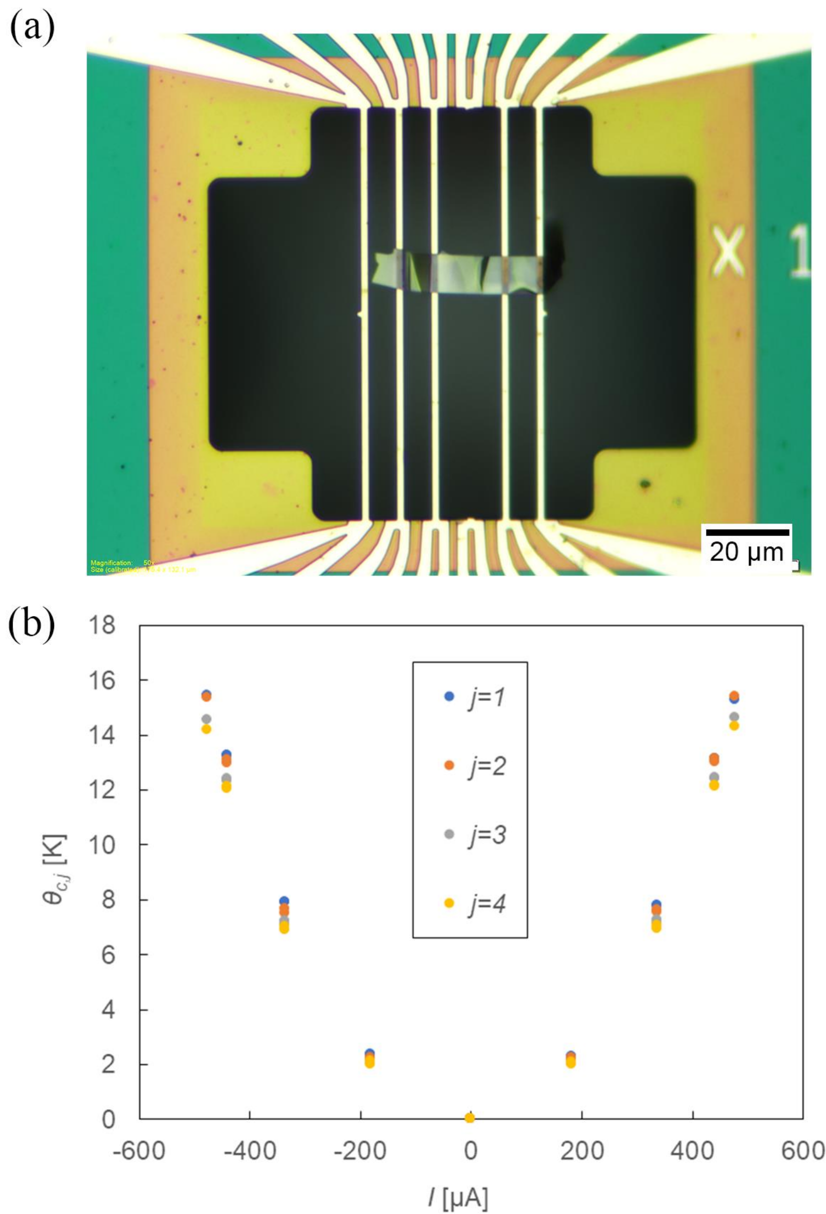

Figure 2.3: (a) Optical micrograph of a 15 μm wide exfoliated graphite ribbon on a four-probe thermal measurement device. (b) Contact point temperature, $\theta_{c,j}$, as a function of the heating current through the first thermometer line. The mismatch between the sample thermal resistance and the device beam thermal resistance results in extremely small contact point temperature differences between thermometer lines.

Matching the sample thermal resistance to the device thermal resistance can be achieved by modifying the geometry and materials used for the device lines, modifying the geometry of the sample, or both. Since the measurement devices are batch fabricated, the thermal resistance of the device lines is tuned to be compatible with the range of sample geometries that can be transferred. The device line thermal resistance is given by $R_{beam} = \frac{L}{4}(\kappa_{SiNx}A_{SiNx} + \kappa_{metal}A_{metal})^{-1}$, where L is the total length of the device beam, A is the cross-sectional area, and κ is the thermal conductivity. The cross-sectional area of both the nitride and metal can be varied to change the thermal resistance of the beam. While the thermal conductivity of the silicon nitride is predetermined based on deposition parameters, the choice of metal for the resistance thermometer line can be used for tuning the beam thermal resistance. Suitable metals for resistance thermometry, such as palladium, platinum, and gold, have different thermal conductivities and can be deposited to thicknesses up to several hundred nanometers.

The thermal resistance of a suspended sample segment is $R_{sample} = \frac{L}{\kappa wt}$, where L is the length of the sample suspended between the device lines, κ is the thermal conductivity of the sample, w is the width of the sample, and t is the thickness of the sample. Without purposefully modifying the thermal conductivity, the sample thermal resistance can only be tuned through changing the sample geometry. For maximum resolution when measuring a sample with a given geometry, such as when studying size dependent effects, the sample thermal resistance can no longer be tuned, and the measurement device must be made to match each sample.

By tuning the device and sample thermal resistances, the measured thermal response has a high signal to noise ratio which results in very small random uncertainty in the final processed data. Figure 2.4 shows the thermal resistances measured for the sample presented in Figure 2.1. The average thermometer line thermal resistance R_b and

the sample thermal resistance R_2 are closely matched for the majority of the temperatures at which the sample was measured. This results in very small random uncertainty in the thermal resistance values and subsequently small random uncertainty in the measured thermal conductivity.

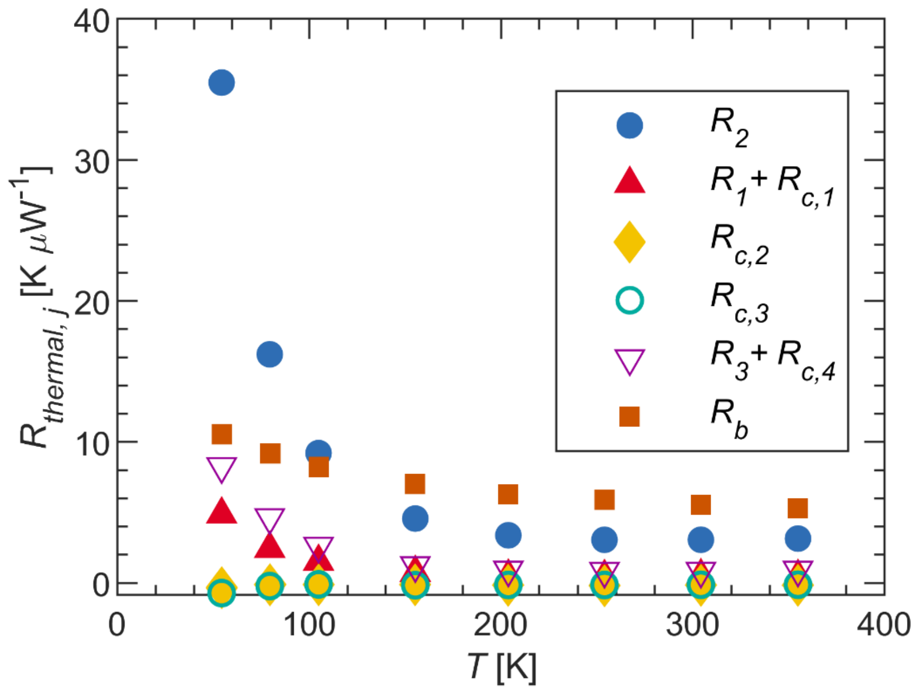

Figure 2.4: Measured thermal resistances of the sample and the average thermal resistance of the thermometer lines. The random uncertainty of the values does not exceed marker size.

Not only should the thermal properties of the device match the thermal properties of the sample, the device geometry must also be appropriate for the intended sample size in order to satisfy the simplifying assumptions. The beam and sample ribbon width should be as small as possible so as not to stray too far from the original assumption of a

point contact between the sample and device.[39] The length of the suspended beams should also be much larger than the width of the sample. Additionally, since the physical property that is being measured is the electrical resistance of the thermometer line, the metal used for the thermometer line as well as the geometry of the thermometer line must be carefully chosen to not only tune the thermal properties of the device, but also the electrical properties. The metal used for the thermometer line should ideally have a strong temperature coefficient of resistance that can be calibrated; metals with a resistivity that is linearly proportional to temperature are the simplest to calibrate and measure. Metals with larger temperature coefficients of resistance and thermometer lines with high resistances will produce larger changes in electrical resistance and have better signal to noise ratios.

2.2.3 Four-Probe Thermal Measurement Micro-Thermometry Device Fabrication

The four-probe thermal measurement devices are batch-fabricated on 4-inch silicon wafers using both additive and subtractive processes. One of the goals of the fabrication process was to completely avoid the use of electron-beam lithography (EBL) for device fabrication due to equipment availability and reliability. While EBL has excellent resolution, far greater than photolithography, the throughput is limited due to serial patterning which has restricted its use in previous devices to only fine features that require the better resolution compared to photolithography.[33,37] All patterning for the devices were done using photolithography which simplifies the fabrication process and allows for good throughput since whole wafers can be patterned all at once. Three different photomasks are used for device fabrication: one to selectively deposit the metal that will act as the contact pads, leads, and device lines, and two to pattern the silicon nitride on the top and bottom of the wafer.

The devices are fabricated on double-side polished silicon wafer that have had low-stress silicon nitride (SiN_x) deposited on both sides. The silicon nitride acts as a support membrane when the device lines are suspended as well as an etch mask during some wet etching steps. The wafers are first cleaned using Piranha solution, a mixture of sulfuric acid and hydrogen peroxide. The Piranha solution removes organic matter, particles, and other contaminants.

Once the wafers have been cleaned, the wafers are then put in an oven that dehydrates the wafers completely and deposits hexamethyldisilazne (HMDS), which acts as an adhesion promoter for photoresist. Photoresist is then spun onto the wafer and a pre-exposure bake evaporates any remaining solvent from the resist.

The metal used in the devices is patterned using a lift-off process where a sacrificial layer is first deposited and patterned in the inverse of the desired design; for these devices, photoresist is used. The target material is then deposited over the entire wafer; the desired target material is deposited directly onto the substrate, while the rest is deposited onto the sacrificial layer. The sacrificial layer can then be removed along with the undesired target material, leaving just the desired pattern.

In the first photolithography step, an image-reversal process is used to create an undercut profile, which creates a clean break in the deposited metal layer and facilitates lift-off. After spinning on photoresist, the inverse of the desired pattern is exposed to UV light using a negative mask. The substrate and exposed photoresist are then baked, cross-linking the previously exposed photoresist and rendering it insoluble in developer. The previously unexposed area remains photoactive. The entire wafer is then flood exposed in UV light, making the previously unexposed area soluble in developer. After developing, the desired pattern with an undercut profile is obtained.

Metal is then deposited onto the wafers using an electron-beam evaporator, covering the entire surface of the wafer. For the devices, a 10 nm adhesion layer of chromium is deposited followed by 120 nm of palladium. The wafers are submerged in heated Remover PG, a solvent stripper, to remove the photoresist and lift-off the undesired metal. After the photoresist has been removed, the wafers are thoroughly cleaned to remove any remaining residues.

To create a fully suspended, etched-through device, the SiN_x on the front and back of the wafers must be patterned to expose the underlying silicon so that it can be etched. To selectively remove SiN_x from the wafers, photoresist is used as an etch mask during plasma etching with sulfur hexafluoride (SF_6) gas. Since photoresist is only being used as an etch mask, the photoresist is exposed normally using a positive mask. After development, the wafers are not post-exposure baked since the unhardened photoresist is sufficiently thick enough to mask the rest of the wafer. Post-exposure baking of the wafer can make the photoresist harder to remove in subsequent steps, leaving potential residues. The wafers are etched using a reactive-ion plasma etcher with SF_6 gas until the exposed SiN_x layer is completely etched through. This process is repeated to pattern the backside of the wafer.

After windows have been etched in the SiN_x on both the front and back of the wafer, the silicon substrate between the two windows is etched completely using tetramethylammonium hydroxide (TMAH) or sodium hydroxide (NaOH). The wafers are etched using a single-wafer wet-etching apparatus that allows the wafer to be etched from only one side. The wafers are etched starting from the backside until they are etched through.

2.2.4 Sample Preparation

The FLG sample presented was exfoliated from a synthetic graphite powder source grown by a high-temperature, high-pressure process by our collaborators in Japan onto silicon wafer pieces with a 290 nm thick silicon oxide layer for optical contrast, which facilitates finding an appropriate sample.[41] After the sample thickness has been measured using atomic force microscopy (AFM), a layer of polymethylmethacrylate (PMMA) is spun onto the wafer piece as a protective layer. Photoresist is then spun on top of the PMMA layer and then patterned using photolithography. The wafer piece is then etched in oxygen plasma, which selectively removes the exposed PMMA and unwanted graphene and graphite flakes. After sample patterning, the remaining PMMA and photoresist are removed in acetone or Remover PG.

The sample can now be transferred onto a suspended measurement device as-is or metal alignment tags can be deposited on top of the sample ribbon to help with sample alignment and improve sample adhesion to the measurement device. To deposit the metal tags, the photoresist and PMMA layers are removed and a new layer of PMMA is spun on. E-beam lithography is then used to expose four slits across the graphene sample ribbon. Metal is then deposited using e-beam evaporation and lift-off.

After completing all processing steps on the sample while it is on a supported substrate, it is transferred onto the measurement device using the procedure shown in Figure 2.5. A PMMA carrier layer is spun onto the wafer piece and then cut into a small rectangle. The wafer piece is then immersed in dilute hydrofluoric acid or buffered oxide etch (BOE) to remove the silicon oxide, releasing the PMMA carrier film along with the patterned sample and alignment marks. The PMMA with the patterned sample can then be rinsed and transferred on a suspended measurement device. The carrier film will naturally float in water and can be picked up using the measurement device. The sample

can be aligned to the lines of the measurement device using a sharp tungsten probe connected to a micromanipulator stage in conjunction with a microscope equipped with high relief objectives. After being picked up by the measurement device, the polymer carrier layer and graphene sample can be manipulated freely while floating on a layer of water. Once the alignment is complete and the sample is allowed time to dry, the polymer carrier layer is removed in acetone, and the sample is dried using a critical point dryer to reduce surface tension effects which can pull together the beams on the measurement device and damage thin-film samples. Without critical point drying, the surface tension of the solvent tends to pull the device beams together and violently release them when the solvent has fully dried, dislodging or tearing delicate samples. After drying, the sample is annealed under high vacuum or forming gas at 350°C to remove any polymer residues remaining on the sample and measurement device. The measurement device is then mounted in a chip carrier using conductive silver paint and wire bonded so that it can be measured in a temperature-controlled cryostat under high-vacuum.

The optical micrograph in Figure 2.1a and scanning electron microscopy (SEM) image in Figure 2.1b show the FLG sample assembled on the four-probe thermal measurement device, which consisted of four suspended Pd thermometer lines deposited on top of a patterned silicon nitride beams. The sample segment suspended between the two middle lines, for which we can find the thermal conductance of, is 3.8 μm wide and 13.0 μm long. Based on AFM measurements of the sample thickness on the silicon wafer prior to the patterning process, the sample is 7 layers thick.

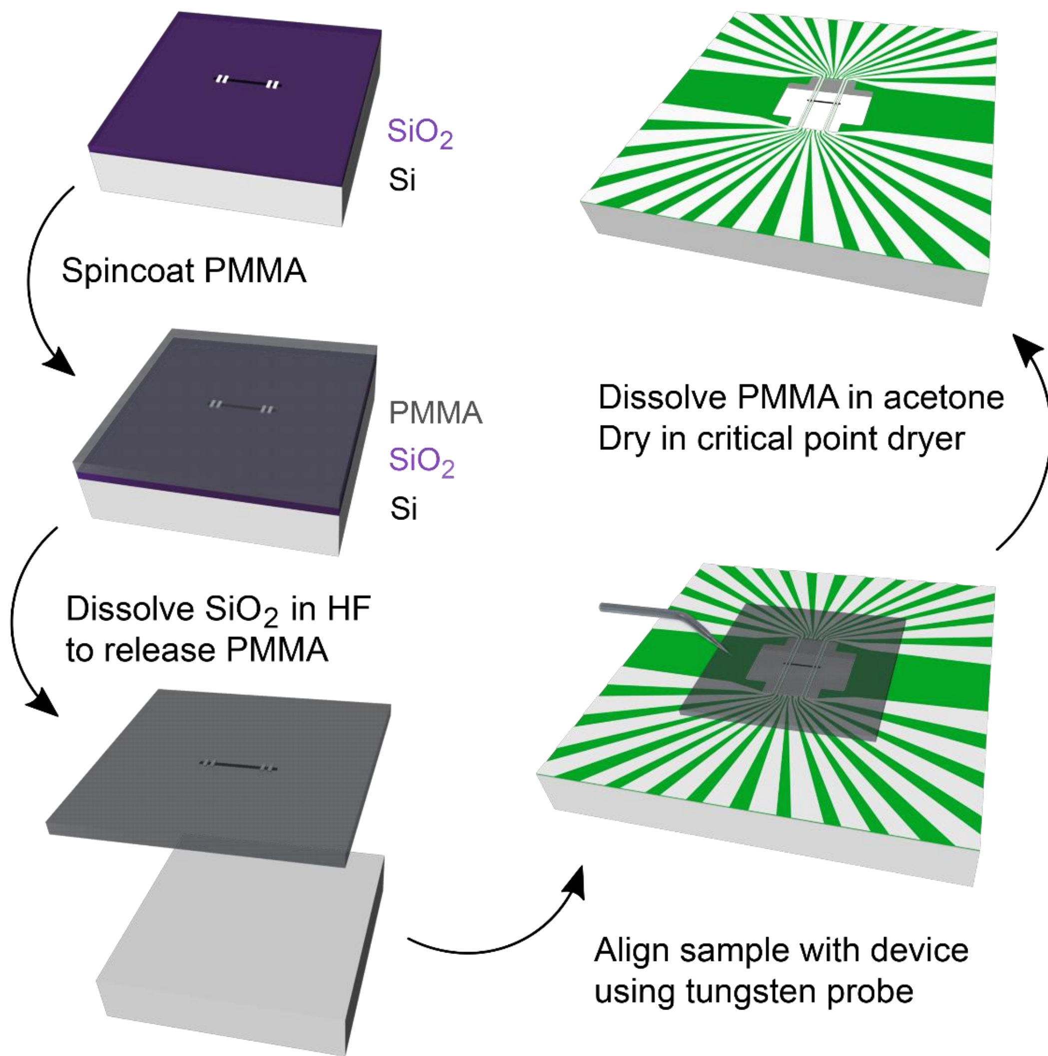

Figure 2.5: Procedure for placing a sample on the measurement device with a polymer carrier layer

2.2.5 Sample Characterization

The sample thickness is measured after exfoliation onto the silicon oxide wafer pieces using atomic force microscopy; the metal tags deposited onto the sample to aid alignment prevents the thickness from being measured accurately after being transferred onto the device. Figure 2.6 shows one of the scans taken of the measured sample along with a plot of the thickness along the dashed line. The thickness of the sample was defined as the average step height of the right edge of the sample taken at multiple points. The dimensions of the final sample ribbon are measured using a scanning electron microscope.

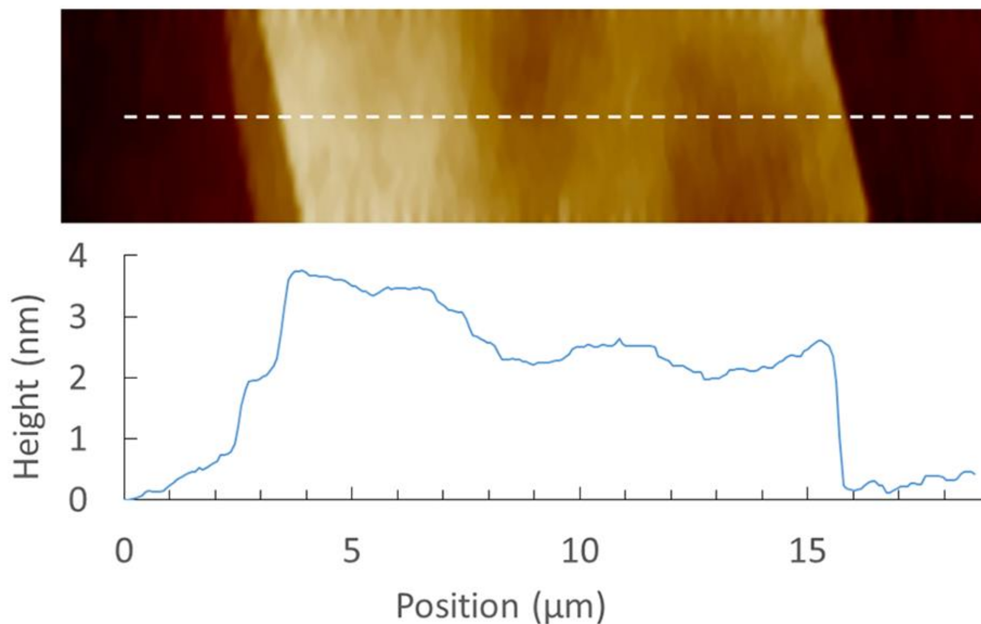

Figure 2.6: Atomic force microscope scan of the 7-layer graphene sample before patterning. The thickness of the sample was determined by averaging the step height measured at multiple points on the right edge of the scan.

Raman spectroscopy is used to verify the sample material and quality. Figure 2.7 shows the Raman spectrum taken with a green laser (532 nm), at low power to prevent burning the sample, on the suspended sample directly on the measurement device. The small bump in the D peak, which may be caused by the edges of the narrow sample, could also indicate that there are some point defects in the sample. The relatively high background signal that increases with increasing Raman shift is indicative of polymer residue left over after transferring the sample.

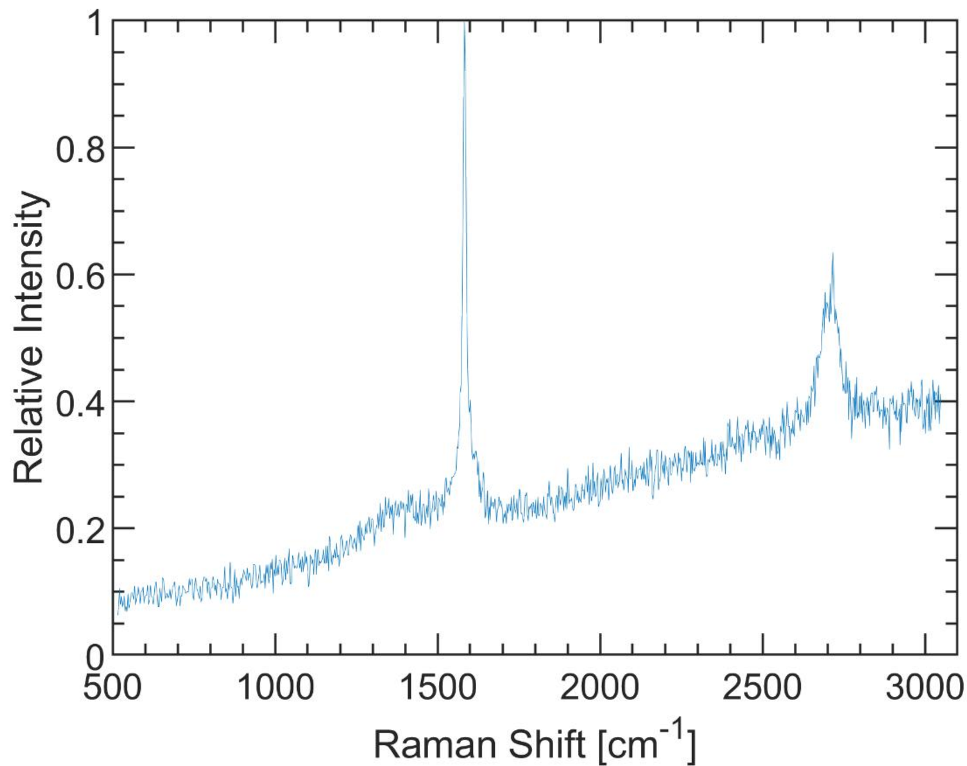

Figure 2.7: Raman spectrum of the middle-suspended segment of the sample.

2.3 RESULTS AND DISCUSSION

The sample was measured in a temperature-controlled cryostat with multiple radiation shields under high vacuum to minimize heat transfer through convection and radiation. Measurements were taken at temperatures ranging from 50 K to 350 K. Figure 2.4 shows the measured thermal resistances of the system at different temperatures. The thermometer line resistance is comparable to the intrinsic thermal resistance of the middle-suspended segment at temperatures above 100K. This condition, which is close to optimum for this comparative thermal measurement, improves the signal to noise ratio in the difference of the measured temperature responses of the two middle thermometer lines.

In addition, the electronic thermal conductance of each metal thermometer line can be obtained from the measured electrical resistance ($R_{e,j}$) and the Wiedemann-Franz law, so that the lattice thermal conductivity of the SiN_x beam under the metal line can be obtained as

$$\kappa_{SiN} = \frac{L}{2A}\left(\frac{1}{R_{b,j}} - \frac{4L_0T}{R_{e,j}}\right)$$

where L and A are the total length and the cross section of each suspended SiN_x beam, L_0 is the Lorenz number, and T is the absolute temperature. The obtained κ_{SiN} range from 3.6-3.8 $Wm^{-1}K^{-1}$ agrees with the literature report for similar low-stress SiN_x.[42]

The directly measured contact thermal resistances (R_{c2} and R_{c3}) of the transferred sample are negligible compared to the intrinsic thermal resistance (R_2) of the middle-suspended segment of the sample. This finding reveals that the four palladium clamps that were transferred together with the FLG were effective in reducing the contact thermal resistance. The ability of separating the contact thermal resistance and directly obtaining the intrinsic thermal resistance here has allowed us to eliminate an important

source of error in the measured thermal transport property. While there have been many methods to reduce the contact thermal resistance, no other methods have been able to measure the contact thermal resistance directly.

The obtained thermal conductivity increases with increasing temperature to reach 503 +/- 21 W m^{-1} K^{-1} at room temperature as shown in Figure 2.8. At room temperature, the value is less than half the highest basal-plane value reported for bulk graphite.[43] In addition, the observed temperature dependence differs from that for high-quality graphite, for which the thermal conductivity peaks at a low temperature near 100 K and decreases with increasing temperature above 100 K due to an increase of intrinsic Umklapp phonon-phonon scattering processes. In comparison, the observed peak temperature is close to 300 K for the FLG sample. This shift of the peak temperature dependence reveals the dominance of extrinsic phonon scattering processes compared to intrinsic phonon-phonon scattering.

One extrinsic scattering mechanism is those by the two side edges and the two end contacts of the suspended middle segment of the few-layer graphene sample. To investigate the impact of side edge and end contact scattering, our collaborators at Pitt University have used first principles calculation to calculate the temperature-dependent thermal conductivity of a suspended single-layer graphene (SLG) sample with a similar width and length.[41] The effects of finite sample size and aspect ratio were included by solving the Peierls-Boltzmann transport equation in both reciprocal and real space domains.[44] Both the temperature dependence and magnitude of the calculation results are much closer to the highest reported thermal conductivity data of high-quality graphite than to the measurement results of the few-layer graphene sample. According to a previous theoretical study,[45] the difference in the thermal conductivity of FLG and SLG of a similar dimension is much smaller than that for the measured FLG sample and the

calculated SLG. These results reveal that side edge scattering and end scattering are not the cause of the reduced thermal conductivity of the 7-layer graphene sample.

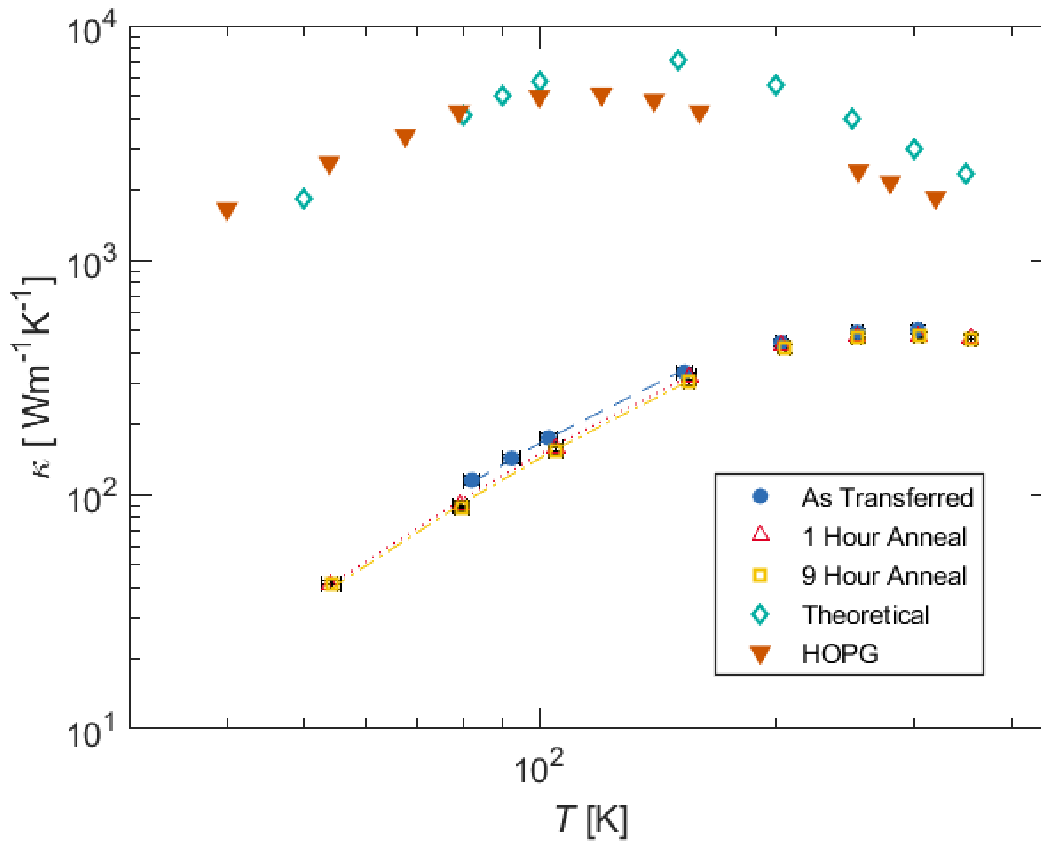

Figure 2.8: Measured and calculated thermal conductivity as a function of temperature. Shown for comparison is the highest basal-plane thermal conductivity reported for bulk graphite included in Touloukian et al. The relaxation time is obtained from a simple scattering model using the specific heat and group velocity calculated from the phonon dispersion of 7-layer graphene and fitting the experimental data. The relaxation time is found to increase with increasing phonon frequency as $\tau^{-1} \propto \omega^{\alpha}$, where α is 0.162, 0.135, and 0.137 for the As Transferred, 1 Hour Anneal, and 9 Hour Anneal measurements respectively. The increasing τ^{-1} with phonon frequency indicates that the intrinsic phonon-phonon scattering is not negligible compared to the extrinsic scattering by polymeric residue.

Other extrinsic scattering mechanisms are point defects and grain boundaries that can be present in the synthetic graphite sample and scattering by the polymer residue left on the top surface of the transferred graphene sample. The presence of polymer residue is clearly revealed in the optical image that shows a dark particle on top of the center region of the middle-suspended segment of the graphene. In addition to this particle, the increased apparent contrast of the graphene sample in the optical image is largely caused by the presence of a residual polymer layer on the suspended graphene sample. As an attempt to reduce the polymer residue, the sample was annealed at 350°C in flowing argon and hydrogen and subsequently re-measured after 1 hour of annealing and again after an additional 8 hours of annealing. However, the annealing did not yield apparent change in either the optical contrast of the FLG sample or the measured thermal conductivity. The Raman spectra measured on the FLG sample after annealing does not show a pronounced D peak that is caused by defects but reveals a background slope that is indicative of the presence of polymer residue. The polymer residue layer increases the mass of the suspended graphene membrane, and impedes both the out-of-plane and in-plane vibration of the graphene atoms,[46] and suppresses the basal plane thermal conductivity contributions from both the in-plane and out-of-plane polarized phonon modes.[31,33]

2.3 CONCLUSION

The four-probe measurement has obtained both the extrinsic thermal contact resistance and the intrinsic thermal conductivity of the 7-layer graphene sample exfoliated from synthetic graphite. As the contact resistance error has been eliminated in this four-probe measurement, the result has allowed us to unambiguously conclude that the observed suppressed thermal conductivity is not due to this measurement error. Our

analysis shows that the suppressed thermal conductivity and the increasing peak temperature are not caused by edge or end scattering that would cause ballistic phonon transport. Instead, scattering by the polymer residue left on the top surface plays an important role, and result in diffusive phonon transport in the suspended few-layer graphene sample. In order to observe non-diffusive thermal transport features including ballistic and hydrodynamic phonon transport that has been predicted to be important in high-quality graphite and graphene,[18,19] it is necessary to first measure a high thermal conductivity that decreases with increasing temperature in the high temperature region where Umklapp phonon-phonon scattering is expected to be dominant. In conjunction with the four-probe thermal transport measurement method reported here, further progress in polymer-free assembly of high-quality graphene samples may lead to eventual observation of intrinsic non-diffusive phonon transport phenomena that have been pursued in experiments over the past two decades.[38]

Chapter 3: Suspended Micro-device Thermometry of Ultrathin Graphite Using Four-Probe Thermal Measurement Method and a Hard Mask Shielded Transfer Technique

3.1 INTRODUCTION

The work in the previous chapter has shown the viability of the four-probe thermal measurement technique for measuring two-dimensional materials; however, the sample assembly procedure involved spin-coating a polymer transfer layer directly onto the graphene sample, leaving hard to remove residue. Previous works have used current annealing,[47] vacuum annealing,[48–50] Ar/H_2 forming gas annealing,[51,52] and O_2 annealing[53] to remove polymer resist residue; however, it has also been shown that some annealing processes, such as annealing in forming gas, fail to completely remove all residue and can in fact produce point defects.[54] After testing the methods that are compatible with our measurement devices and available equipment, we found that there was no appreciable difference before and after annealing our thin-film samples after transfer. The residue can scatter the ZA phonons of the suspended sample and suppress thermal conductivity.[33] Previous observation of a high-temperature peak thermal conductivity is indicative of extrinsic scattering processes affecting the ability to measure intrinsic thermal performance.

In order to observe intrinsic phonon transport phenomena such as hydrodynamic phonon flow in graphene, a clean sample preparation method must be established. This chapter describes a method to reduce direct polymer contamination of thin-film samples when using the four-probe thermal measurement technique. The method utilizes a hard mask to shield the sample from direct contact with polymer films used during sample preparation.

3.2 Experimental Method

3.2.1. Sample Preparation

Whereas the previously reported thin-film sample was processed and then transferred onto a fully suspended measurement device, the sample preparation used in this chapter is integrated with the final fabrication steps of the measurement device. The sample preparation and device fabrication steps are largely the same as before except the sample is protected from direct polymer contamination with a prefabricated silicon oxide beam and transferred onto a partially supported device. These changes necessitate shifting the order of some of the sample assembly steps.

The sample assembly process starts the same as before; a graphite source is exfoliated onto a silicon substrate that has approximately 300 nm of thermally grown oxide for optical contrast as shown in Figure 3.1a. The oxide substrate is surveyed for flakes of the appropriate size and thickness. The thickness is then measured using AFM on the oxide substrate since, like previously, it cannot be measured after it has been transferred onto the device.

After a suitable sample has been identified and characterized, a prefabricated oxide beam is transferred on top of the desired graphene flake using a sharp tungsten probe as shown in Figure 3.1b. The oxide beam shields the graphene flake from direct polymer contact and serves as a hard mask for sample etching; therefore, the oxide beam should be the same length and width as the desired sample ribbon. The oxide beam is also used to align the sample with the measurement device during wet transfer. The oxide beam is made by patterning a wafer with thermally grown oxide using either EBL or photolithography and then etched using CF_4 or SF_6 plasma. Beams of various lengths and widths are patterned to accommodate different sample sizes and allow for some tuning of

the sample conductance. The beams are then suspended by etching the silicon substrate using TMAH so that they can be readily picked up using a sharp tungsten probe. A layer of titanium or aluminum is then deposited on top of the beams using e-beam evaporation for increased contrast to facilitate sample alignment during transfer. Titanium and aluminum were chosen since both can be easily removed using hydrofluoric acid, which does not damage the rest of the measurement device.

Previously, photolithography was used to selectively etch the sample flake into a ribbon shape, which involved spin-coating a polymer film directly on top of the sample. For this sample assembly process, the oxide beam acts as a hard mask for the sample patterning. After the oxide beam has been transferred on top of the sample flake, the unwanted portion of the sample, which is not covered by the oxide beam, is etched using O_2 plasma as shown in Figure 3.1c. After patterning the sample, a layer of PMMA is spun onto the silicon substrate and the sample is then transferred onto a partially supported measurement device using the wet transfer method described in the previous chapter. The partially supported measurement devices have had all process steps completed except for the etching of the silicon substrate to suspend the device lines. Figure 3.1d shows an oxide beam and graphene sample stack that has been transferred onto a supported device.

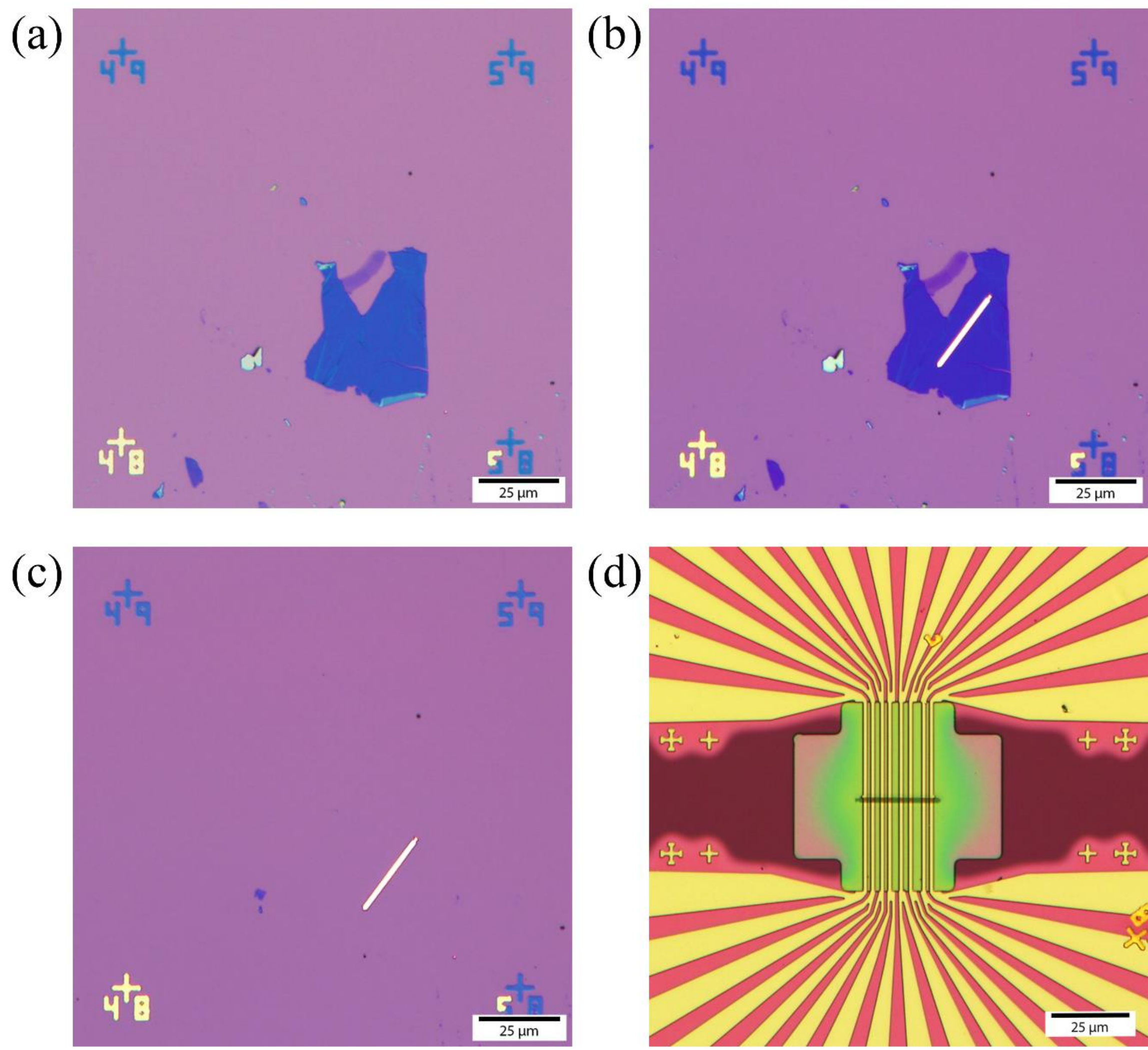

Figure 3.1: (a) Natural graphite flake exfoliated onto a silicon wafer with 300 nm thermally grown silicon oxide (b) Prefabricated oxide beam that has been transferred onto the exfoliated flake (c) Oxide beam and graphite flake after O_2 plasma etching. The oxide beam serves as a hard mask for the dry etching process. (d) Graphite flake and oxide beam that have been transferred together onto eight thermometer lines supported on a Si substrate using a PMMA transfer film.

After transferring the graphene and oxide beam stack onto the supported measurement device, several EBL steps are performed on the PMMA transfer film in order to anchor the oxide beam to the measurement device. Without any anchors, it is possible for the oxide beam to be washed away when removing the PMMA used for sample transfer, contaminating and possibly physically damaging the sample in the process. Due to the thickness of the PMMA transfer film, one EBL exposure is dedicated to removing the PMMA on top of alignment marks which would be otherwise difficult to see under the thick transfer PMMA. After developing the EBL pattern, another EBL step is used to expose narrow slits above where the sample ribbon and device lines intersect. Dilute hydrofluoric acid is then used to round the edge on top of the oxide beam so that a conformal layer of metal forms during metal evaporation on the sample. Finally, a third EBL step is used to widen the slit to the full width of the device line and to extend the length of the window so that it is several microns longer than the width of the oxide beam as shown in Figure 3.2a. Metal is then deposited in an e-beam evaporator with the sample placed at the edge of the deposition platter to ensure that the oxide beam is anchored by conformal contact on at least one side of the beam. At this point, the PMMA used for wet transfer is finally removed to lift-off the unwanted metal and the final result can be seen in Figure 3.2b.

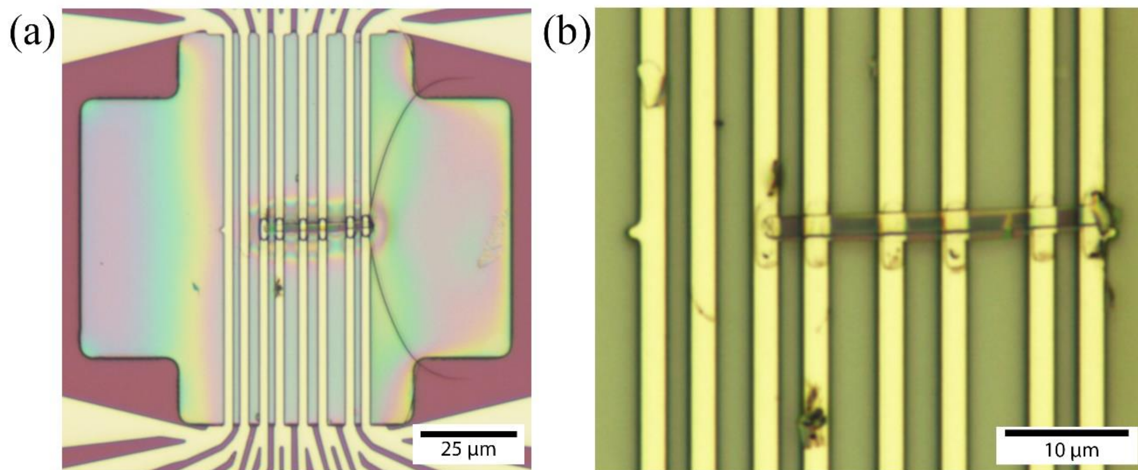

Figure 3.2: (a) Optical micrograph of sample assembly procedure after all e-beam lithography steps. This representative sample is ready for metal deposition. (b) Optical micrography of the oxide beam after metal lift-off. The metal that has been selectively deposited helps to anchor the oxide beam when the PMMA transfer film is removed.

Once the oxide beam is anchored, the fabrication of the device is completed by suspending the device lines by etching the silicon substrate using either TMAH or KOH. After the device lines are suspended, the oxide beam is removed using BOE or dilute hydrofluoric acid. The sample and device are then rinsed and stored in deionized water or isopropanol until the sample can be dried in a critical point dryer. After drying, samples are annealed in forming gas at elevated temperature to remove any residue left from the critical point dryer.

3.2.2 Multi-Probe Thermal Measurement Method

Previously, suspended lines in the completed devices could be selectively broken to change the lengths of the suspended sample segments to match the exfoliated sample flake size; however, since the devices used for the updated sample assembly procedure have not had their device lines suspended before sample transfer, it is not possible to

change the device line spacing without using a different photomask. The mask designs used for making the four-probe thermal devices currently have eight lines. Examining the thermal circuit shown previously in Figure 2.1c, we can see that it is possible to expand the analysis to any number of device lines, n, greater than 4, with $n-3$ number of intrinsic sample segments that can be measured for any given sample. Figure 3.3 shows the thermal circuit for using the four-probe thermal measurement method with eight lines. Due to the possibility of the failure of any individual sample segment and the need for the sample to bridge four lines uninterrupted, it is beneficial to maximize the number of device lines bridged by the sample to increase overall sample yield. While it would be ideal to be able to measure a sample that bridges all eight lines, which would allow us to measure the intrinsic conductance of five suspended sample segments from the same exfoliated flake, if any sample segment breaks, it would still be possible to measure the sample as long as the sample bridges more than four lines uninterrupted.

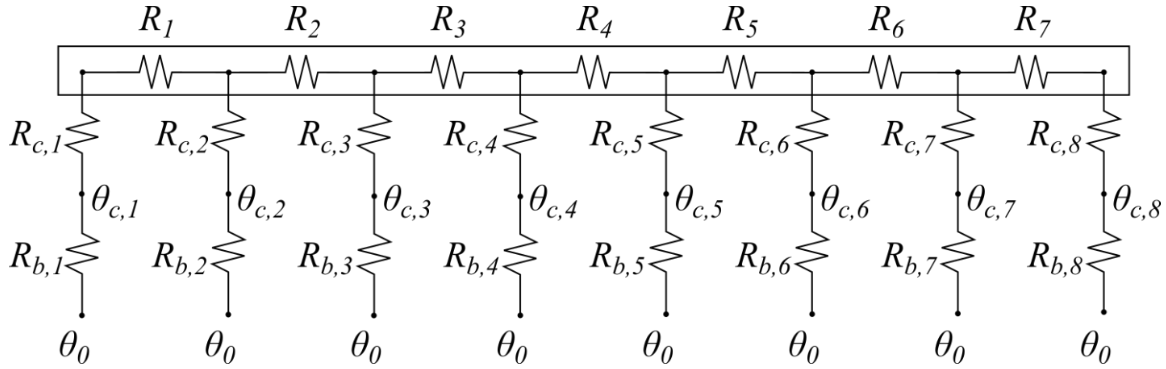

Figure 3.3: Thermal circuit for a sample assembled across a measurement device with eight suspended thermometer lines. The thermal resistance of each of the sample segments suspended between device lines are represented by $R_{s,n}$ for $n=1$ to 7. At each sample and device interface, there is some contact resistance between the sample and the jth line, $R_{c,j}$. Each device beam has some thermal resistance, $R_{b,j}$, for the jth beam. Each device beam is thermally grounded into the device substrate and maintains a temperature rise above sample stage temperature of $\theta_0=0$. $\theta_{c,j}$ is the temperature rise above sample stage temperature of the jth device line at the sample contact point.

3.3 Results and Discussion

Two ultrathin graphite samples were assembled onto the four-probe thermal measurement device using the oxide beam hard mask. The graphite samples were exfoliated from natural graphite due to the high yield of suitable samples which facilitates the process development for the new transfer and sample assembly process. The samples presented here are 7.71 nm and 7.37 nm thick. The 7.71 nm thick sample, shown in Figure 3.4 (a) and (b) was patterned using an oxide beam that was 45 µm long and 3.7 µm wide and transferred across eight lines of the measurement device. This sample broke during the four-probe thermal measurement; the crack in the sample can be seen in Figure 3.4b, a scanning electron micrograph taken after measurement. Once it was confirmed that there was no electrical or thermal signal between the 4th and 5th device lines, which is shown in Figure 3.5, plots of the change in sensing line resistance between lines with

damaged and undamaged suspended sample segments, the two halves of the sample were measured separately and treated as two samples spanning four device lines each with middle suspended sample segments lengths of 3 µm and 5 µm respectively. The 7.37 nm thick sample was patterned using a 25 µm long and 1.7 µm wide SiO_2 beam and transferred across four lines of a measurement device as shown in Figure 3.4 (c) and (d) and has a middle-suspended segment length of 5 µm.

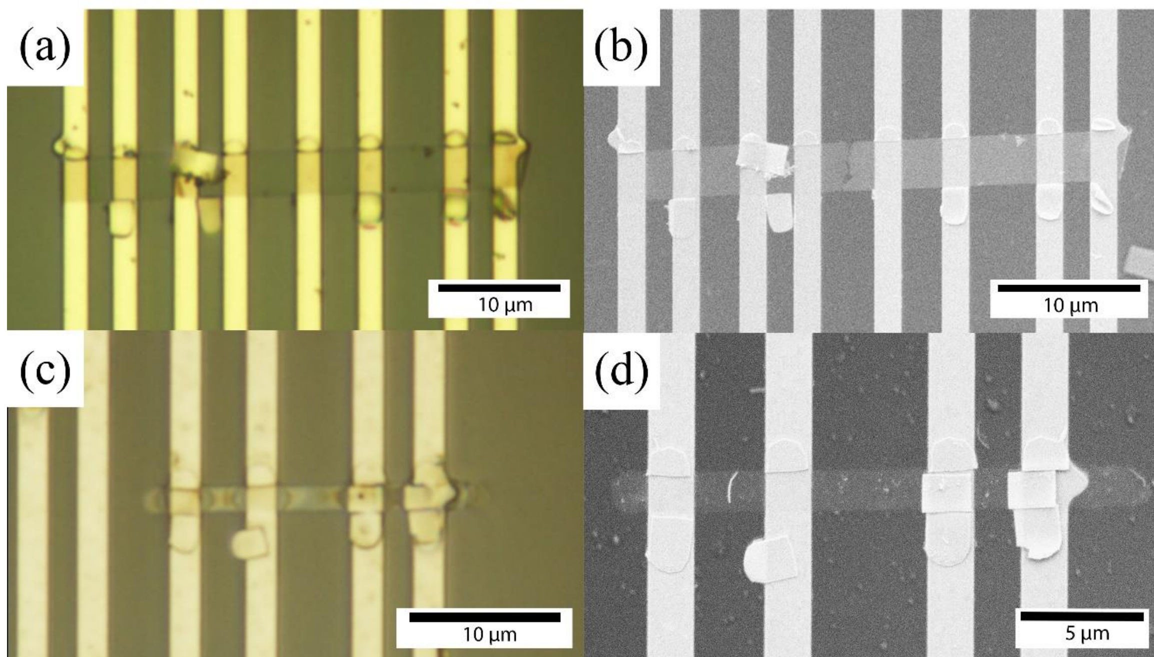

Figure 3.4: (a) Optical and (b) scanning electron micrographs of a 7.71 nm thick sample that has been patterned into a 45 µm long and 3.7 µm wide ribbon and transferred across eight lines of the four-probe thermal measurement device. (c) Optical and scanning (d) electron micrograph of a 7.37 nm thick graphite sample transferred onto four lines of a four-probe measurement device.

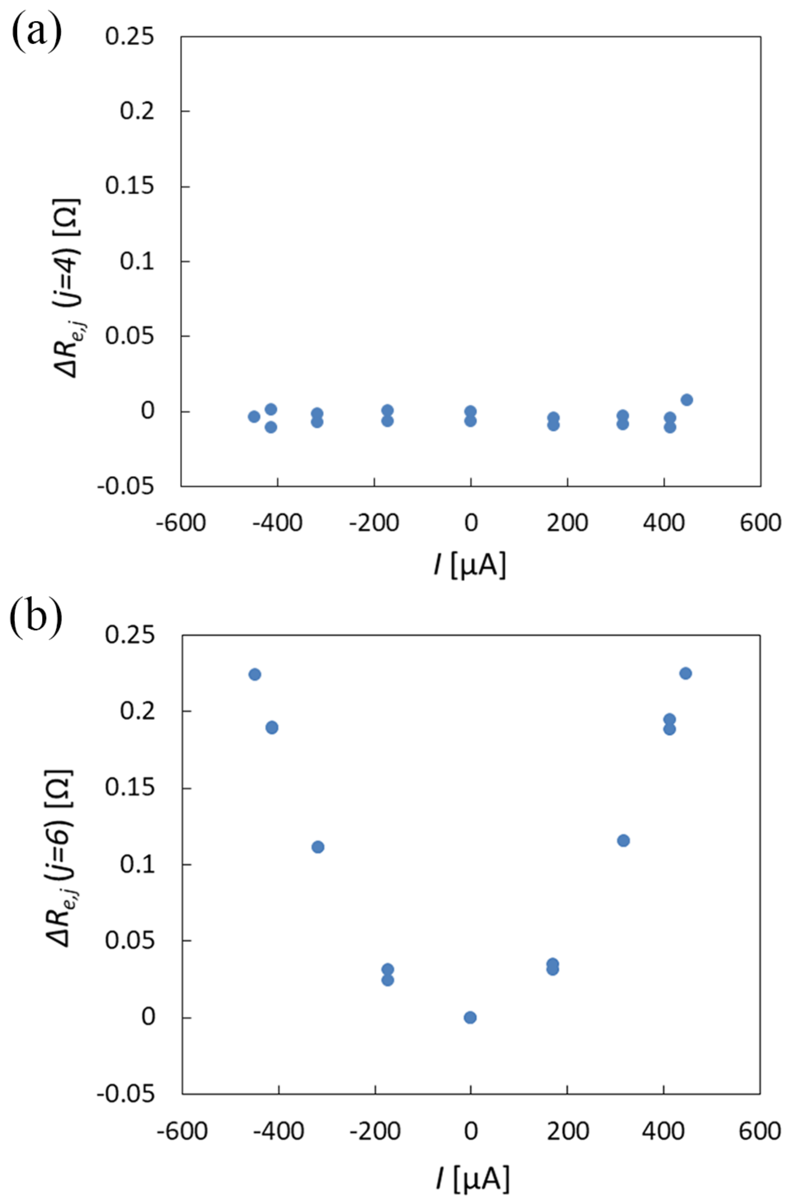

Figure 3.5: Change in electrical resistance of the jth sensing line vs heating current in the 5th line for $j=4$ (a) and $j=6$ (b) of the 7.71 nm thick sample transferred across eight lines. The suspended sample segment between the 4th and 5th lines was damaged during measurement, resulting in no heat flow between those lines.

The samples were measured in a cryostat under high vacuum at sample stage temperatures ranging from 80 K to 350 K. Since the eight-line sample broke in the middle, we are only able to measure the intrinsic thermal conductivity of two of the suspended sample segments, the segments between the 2nd and 3rd lines from the left and 6th and 7th lines of the sample shown in Figure 3.4 (a) and (b). The thermal conductivity of these two middle suspended sample segments is presented in Figure 3.6 along with the middle-suspended segment of the sample shown in Figure 3.4 (c) and (d). The peak thermal conductivity of the samples presented in this chapter is 706 $Wm^{-1}K^{-1}$ for the 7.71 nm thick, 3 μm long sample at 275 K. The slightly thinner 7.37 nm sample shows a lower peak thermal conductivity of 501 $Wm^{-1}K^{-1}$ at 325 K.

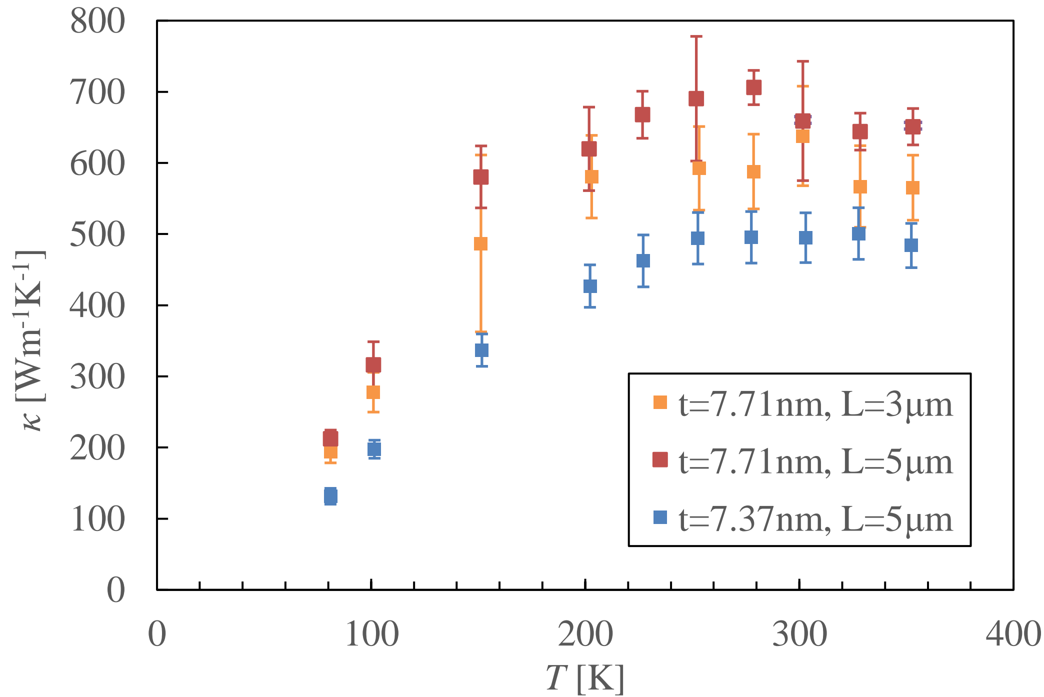

Figure 3.6: Measured thermal conductivity as a function of temperature for three suspended natural graphite samples of various thicknesses and lengths.

While the thermal conductivities of the samples presented in this chapter are higher than the thermal conductivities of the few-layer graphene sample presented in the previous chapter, it is difficult to make direct comparisons due to the different source materials from which the flakes were exfoliated as well as the large differences in sample thicknesses. The thermal conductivities reported here are still much lower than those predicted by theoretical calculations for high quality graphite and graphene, indicating defects in the sample and possibly polymer contamination during the sample assembly.

To investigate whether the low measured thermal conductivities of the samples obtained from exfoliating natural graphite were due to a batch of poor quality source material or contamination during the sample assembly process, additional samples were prepared using a commercially available highly oriented pyrolytic graphite (HOPG) source using the same assembly process as the natural graphite samples. One of the prepared HOPG samples, shown in Figure 3.7, has very comparable dimensions to the natural graphite samples; the HOPG sample is 21-layers thick and has a middle-suspended sample segment length of 5 μm.

Like the exfoliated natural graphite samples, the HOPG sample was measured in a temperature-controlled cryostat under high vacuum. The measured thermal conductivity of the HOPG sample is very comparable the previously measured natural graphite samples and similarly exhibits a high temperature peak thermal conductivity as shown in Figure 3.8. These results suggest that all samples might still have been contaminated during the transfer process, thus suppressing the measured thermal conductivity. Another possibility is that ripples, which can suppress phonon transport,[55] have formed in the suspended sample. Further structural analysis is needed to understand the exact cause of the suppressed thermal conductivity and increased temperature of the thermal conductivity peak.

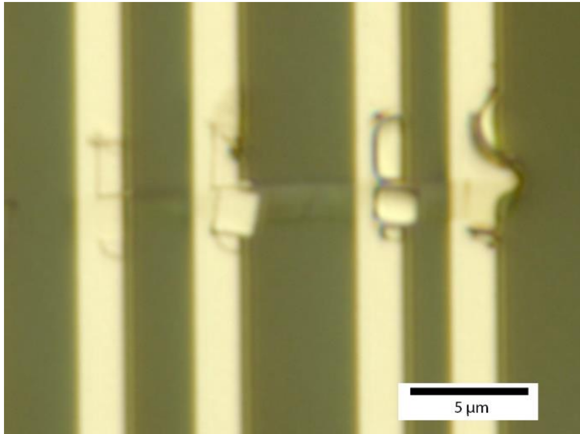

Figure 3.7: Optical micrograph of 7.04nm thick sample exfoliated from high oriented pyrolytic graphite patterned into an 18 µm long, 1.7 µm wide ribbon and transferred across four lines of a four-probe thermal measurement device.

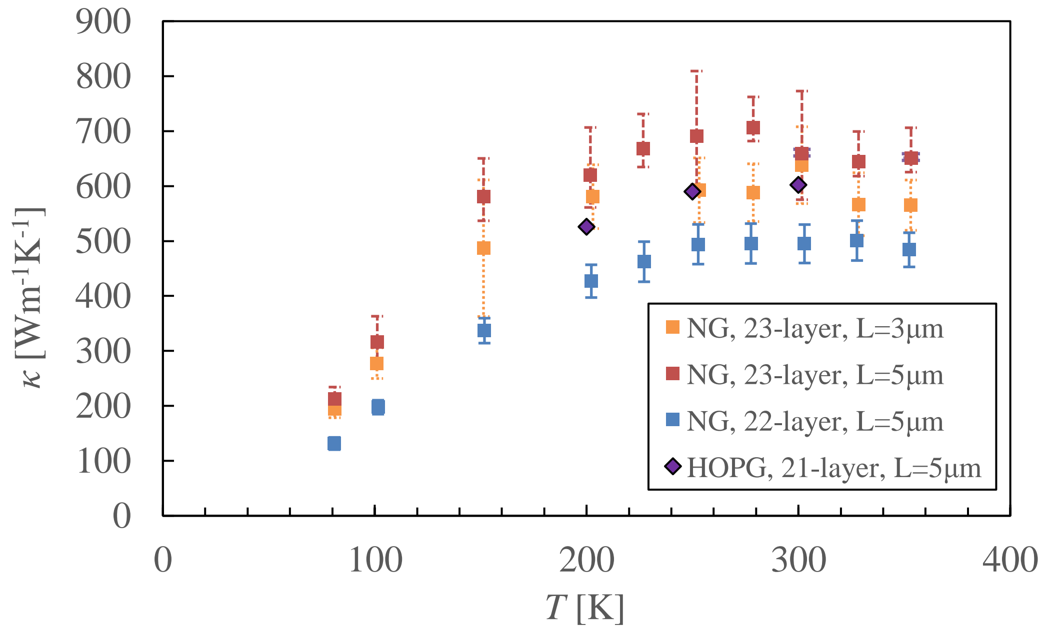

Figure 3.8: Measured thermal conductivity as a function of temperature of the exfoliated highly oriented pyrolytic graphite (HOPG) sample compared to three exfoliated natural graphite (NG) samples.

Although the topside of the sample is shielded from direct polymer contact by the oxide hard mask, there are still several process steps in which the sample can be contaminated. The scale cross-section drawing of the sample assembly depicted in Figure 3.9 shows that once assembled on the partially supported device, the sample and oxide beam stack are only supported by the device lines. The empty space between the device lines form trenches whose depth is at least equal to the combined thickness of the deposited metal layers and silicon nitride. Over etching during the nitride plasma etching step can damage the silicon underneath the nitride that was removed, creating even deeper trenches. The PMMA used during wet transfer has poor adhesion to the partially supported measurement device, even after baking. During development of EBL exposure, polymer contaminated solvent can enter the trenches between the device lines and leave residue on the underside of the sample.

Figure 3.9: Scale drawing of a sample that has been transferred onto a partially supported measurement device. All EBL steps have been performed and the assembly is ready for metal deposition. The supported device consists of the silicon substrate (gray), nitride beams (green) and contact metal (silver). The sample and oxide beam (purple) have been transferred onto the device using a PMMA carrier layer (blue), which has been patterned using EBL. The sample is attached to the bottom of the oxide beam and is not in direct contact with any polymer layers.

The Raman spectrum of the middle-suspended segment of one of the samples, shown in Figure 3.10, is representative of samples measured in this chapter. The weak response from suspended samples measured using low laser power combined with the rough surface of the shallow trench etched underneath the samples to suspend the device lines leads to a noisy signal with a large background. While the large background signal of the FLG sample in the previous chapter was attributed to polymer residue, it is unclear whether the large background signal is caused by polymer residue or due to the uneven surface left from etching the silicon from only the topside of the device.

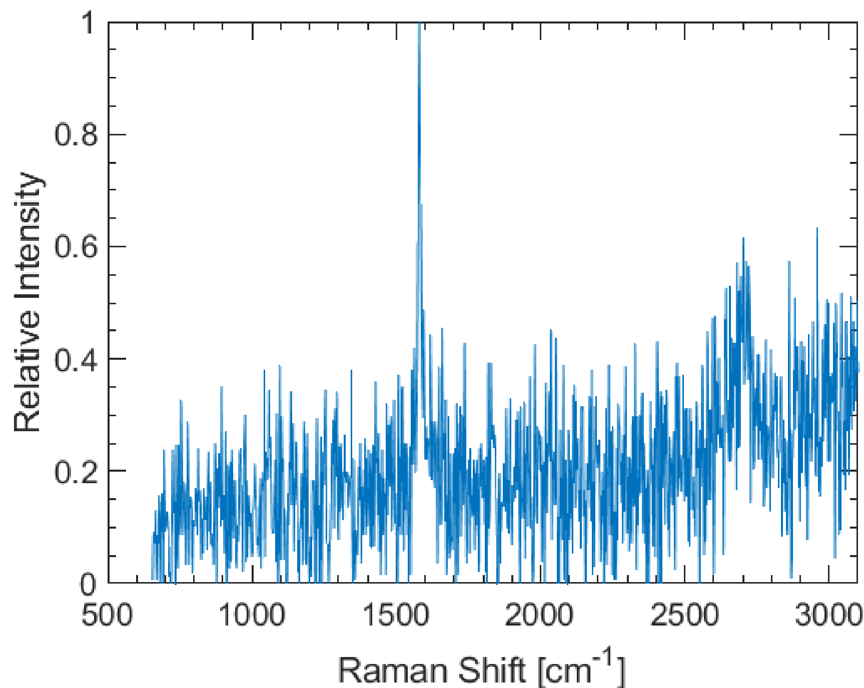

Figure 3.10: Raman spectrum of the middle-suspended segment of the 7.71 nm thick, 5 μm long sample.

3.4 CONCLUSION

A cleaner sample transfer method has been used for sample assembly on the four-probe thermal measurement device to measure two exfoliated natural graphite samples and one exfoliated HOPG sample. While no polymer layer is spun on and baked directly onto the samples, it is still possible for polymer residue to contaminate the underside of the samples through the uneven surface of the partially supported devices. The samples measured here have higher thermal conductivities than to the sample presented in the last chapter; however, the thermal conductivities measured are still much lower than expected from theoretical calculations as well as compared to other experimental results. Additionally, a high thermal conductivity that decreases with increasing temperature in the high temperature region where Umklapp phonon-phonon scattering is expected to be dominant has not been observed so further progress in assembling clean, high-quality graphene samples is needed in order to observe intrinsic, non-diffusive phonon transport phenomena such as hydrodynamic phonon transport. Further atomic force microscopy, scanning electron microscopy, and transmission electron microscopy analyses are needed to understand whether the suppressed thermal conductivity and increased temperature of the thermal conductivity peak are caused by polymer contamination on the bottom of the sample, ripples formed in the suspended sample, or defects in the source materials.

Chapter 4: Fabrication of a Fully Supported Four-Probe Thermal Measurement Device Using a Vertically Embedded Sacrificial Oxide for Clean Transfer of Graphene Samples

4.1 INTRODUCTION

Although the sample assembly procedure presented in the last chapter avoided direct contact between the sample and polymer film, it is was still possible for polymer residue to contaminate the sample surface, preventing the measurement of the true intrinsic properties of the thin-film samples. In this chapter, a method to vertically embed a sacrificial oxide on the supported four-probe measurement devices to create a fully supported, flat substrate is reported. This flat substrate, combined with the oxide beam hard mask transfer method used in the previous chapter can shield both sides of the thin-film samples to prevent the ingress of polymer residue as well as make the four-probe measurement device compatible with other thin-film transfer methods that do not rely on polymer carrier films.

4.2 DEVICE FABRICATION AND SAMPLE ASSEMBLY

4.2.1 Introduction

While the previously presented sample assembly technique prevented direct contact between the sample and polymer transfer film, the underside of the sample was still susceptible to polymer contamination during EBL steps while assembled on the partially supported measurement device. Deep trenches between the device lines and poor adhesion of the polymer transfer film allowed the solvent used for developing EBL exposures to wick into the trenches between the lines via capillary action. The solvent eventually evaporates, leaving behind polymer residues on the underside of the sample.

The sample assembly procedure presented here employs a scaffolding technique that has previously been used to assemble delicate carbon nanotubes onto a suspended measurement device.[56] In this technique, an array of trenches is etched into the nitride film of a silicon/silicon nitride wafer. The trenches are then embedded with a sacrificial silicon oxide to create a flat surface. This filled trench is designed to be a sacrificial layer between two membranes of a thermal conductance measurement device that will fully support the sample during fabrication. Carbon nanotubes were then transferred onto the wafer and samples in suitable positions will have devices patterned around them.

In the technique presented here, we employ a similar sacrificial layer of oxide that will fill in the gaps between the nitride and metal device beams and provide a flat surface on which the sample can be transferred. The flat surface will improve sample adhesion and prevent the ingress of polymer residue when developing e-beam lithography exposures. If the sample adhesion is sufficient, then the PMMA may even be removed without washing away the oxide beam and sample, making the e-beam lithography steps for fabricating the metal clamps used in previous chapters unnecessary.

Adding the vertically-integrated sacrificial oxide and transforming the four-probe thermal measurement device into a flat substrate also makes the devices compatible with many more sample transfer techniques compared to the suspended and partially supported devices used in the previous two chapters, many of which do not rely on a polymer carrier film. One of the major approaches that has been used extensively for graphene transfer is based around elastomer stamps.[57–60] In this approach to sample transfer, an elastomer pad, typically made out of polydimethylsiloxane (PDMS), is pressed against chemical vapor deposition (CVD) grown graphene on a metal foil. The metal foil is then dissolved, leaving the graphene on the PDMS, which can then be stamped onto a flat substrate and then gently removed, leaving the graphene on the

substrate. This method requires the adhesion between the graphene and destination surface to be stronger than that between the graphene and PDMS, limiting its applicability to hard, flat, and hydrophilic surfaces.[57]

Several variations on the basic PDMS stamping technique have expanded its capabilities to a wider variety of target substrates and materials which can be transferred. The general reliability of the PDMS stamping method has been improved through the use of a self-release layer, which is inserted between the elastomer stamp and the graphene sheet.[61] The low adhesion between the stamp and the release polymer compared to the graphene and the destination surface allows the graphene to be transferred to soft surfaces. Whereas the previously mentioned PDMS stamping techniques are primarily used only for CVD grown graphene on metal foil, a recently developed technique, which utilizes a hemispherical handle substrate, has the ability to transfer exfoliated flakes between different substrates.[62] In this technique, a hemisphere made from epoxy or PDMS is coated with polypropylene carbonate (PPC), an adhesion-improving polymer, and then used to pick up an exfoliated flake. The flake is aligned with the target substrate and the hemispherical handle pressed against the substrate at elevated temperature, allowing the PPC to detach from the hemispherical handle.

4.2.2 Method

To create the vertically embedded sacrificial oxide layer, silicon oxide is sputtered onto the device wafers after the contact metal and silicon nitride window have been patterned. The silicon oxide will be deposited on the entire surface of the wafer, filling in the trenches between the device lines as well as covering the device lines themselves. Chemical mechanical planarization (CMP) will then be used to remove the oxide over the device lines so that the samples can have good thermal contact with the device. CMP will

also flatten the wafer at the same time to provide a hard, flat target area onto which the sample is transferred.

Although only minor changes were needed to shield the topside of the graphene sample using the oxide beam, fundamental changes to the fabrication process need to be made in order to be compatible with the CMP process. Figures 4.1 and 4.2 depict different views of the basic fabrication sequence. A sacrificial metal layer is deposited on top of the metal used for the thermometer lines for protection during CMP. Since it is difficult to make the CMP process selectively etch only the oxide, the total metal thickness is greater than what can feasibly be achieved using photolithography and metal lift-off. As a result, a sputtering service is used to deposit metal onto the bare silicon/silicon nitride wafers which will then be patterned using a subtractive etching process instead of the additive lift-off process used previously. After depositing the metal on top of the bare wafers, a layer of silicon oxide is deposited for use as a hard mask during physical plasma etching of the metal. Photolithography is used to pattern the silicon oxide on top of the metal using SF_6 plasma etching. Once the oxide has been patterned, the photoresist is removed, and the patterned oxide is used as a hard mask to pattern the metal layer using argon plasma. The nitride window is then patterned using photolithography and dry etching using the self-aligned process as before. Once the contact metal has been patterned along with the nitride window used for suspending the device, silicon oxide is once again sputtered onto the entire top surface of the wafer to fill in the trenches between the device lines. The wafers are then abraded using a CMP process until the device lines are exposed and the substrate is flat.

After CMP has created a flat, fully supported measurement device, the samples are ready to be transferred using the oxide beam method described in the previous chapter. The filled trenches will support the sample completely while the oxide beam

protects the top of the sample. If necessary, metal tags are deposited to anchor the oxide beam so that it does not wash away during the removal of the PMMA transfer film. Once the PMMA has been removed, the oxide is etched using HF vapor and the silicon is etched using XeF_2 gas. Since both the silicon oxide and silicon etching steps use a vapor etching process instead of a liquid etching process, critical point drying is not necessary, eliminating another potential source of contamination.

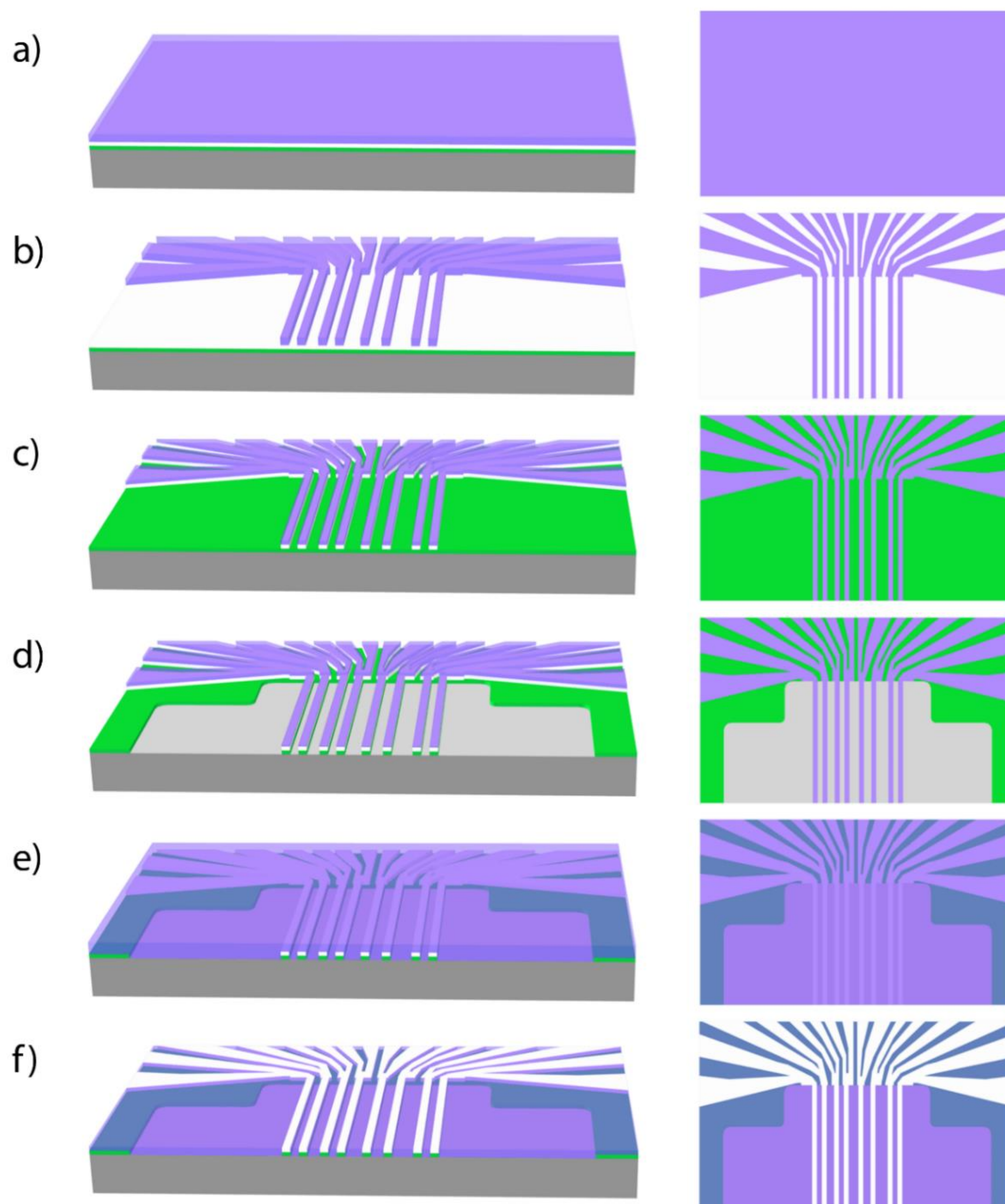

Figure 4.1: Orthographic and top views of the fully supported four-probe thermal measurement device fabrication. (a) Silicon substrate (gray), with deposited silicon nitride (green), sputtered metal (silver), and sputtered silicon oxide (purple). (b) Silicon oxide hard mask is patterned using photolithography and dry etching. (c) Metal layers are patterned using the silicon oxide hard mask and dry etching. (d) Silicon nitride window is patterned using photolithography and dry etching. (e) Silicon oxide is sputter onto the wafers, acting as vertically embedded sacrificial oxide. (f) CMP of sacrificial oxide to create flat substrate.

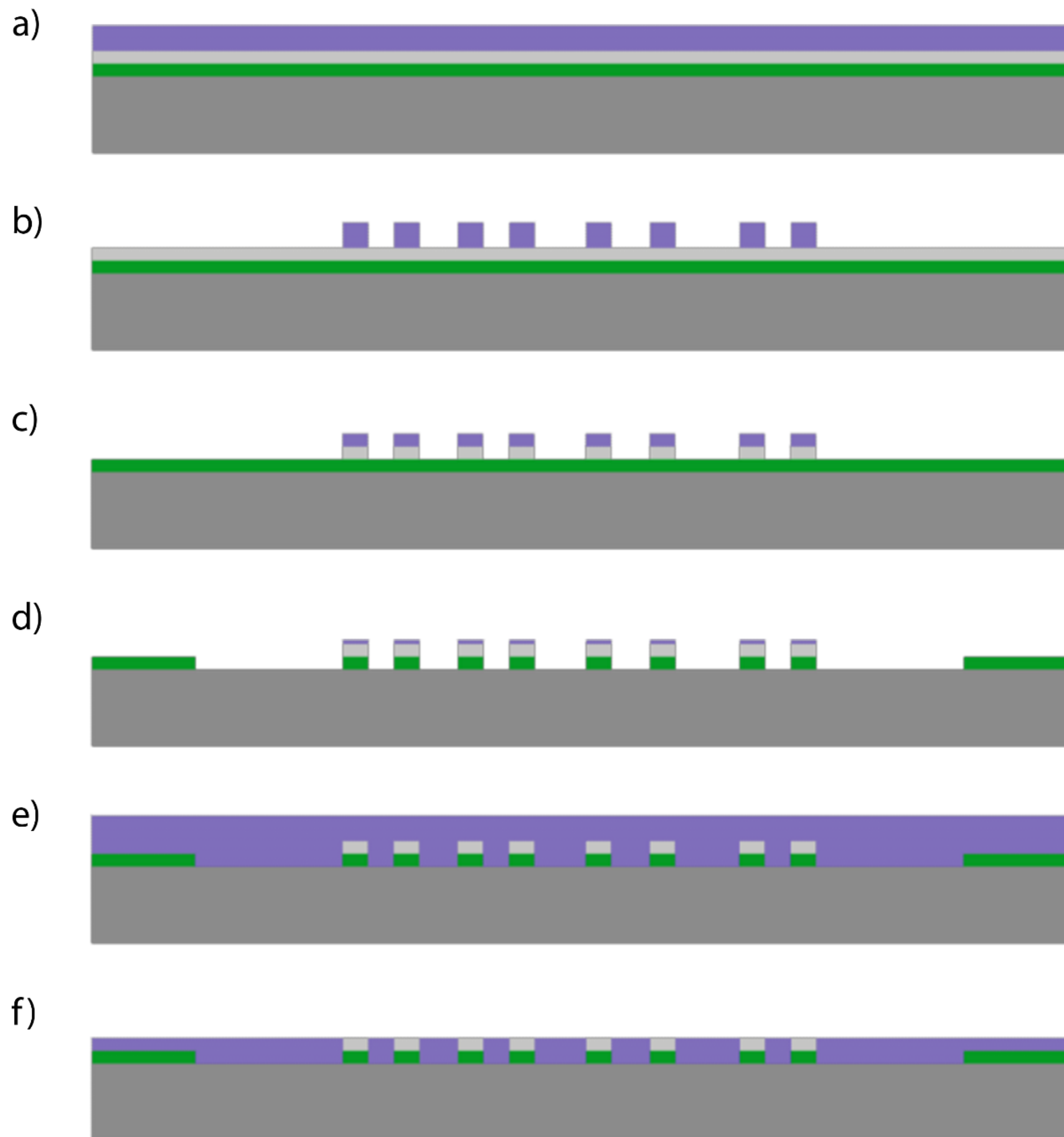

Figure 4.2: Partial cross-section view of sacrificial oxide layer fabrication around the device lines of the four-probe thermal measurement device. (a) Silicon substrate (gray), with deposited silicon nitride (green), sputtered metal (silver), and sputtered silicon oxide (purple). (b) Silicon oxide hard mask is patterned using photolithography and dry etching. (c) Metal layers are patterned using the silicon oxide hard mask and dry etching. (d) Silicon nitride window is patterned using photolithography and dry etching (e) Silicon oxide is sputter onto the wafers, acting as vertically embedded sacrificial oxide. (f) CMP of sacrificial oxide to create flat substrate.

4.2.3 Challenges

While this new method has many advantages over the previously reported sample assembly techniques, the added complexity of the new process creates new challenges. Due to the lack of availability of certain equipment or the incompatibility of the current equipment with the requirements of the new process, many of the steps, such as the metal sputtering, oxide sputtering, and vapor etching steps, will need to be performed at other facilities. For the CMP process, the chemical and mechanical elements of the planarization process need to be balanced so that the metal layer and sacrificial oxide layer ultimately form a completely flat surface. Any irregularities at the interface between the two materials can lead to complications which can damage the sample during transfer or create avenues for polymer contamination. The CMP process, in additional to non-uniform removal of material at the device scale, often removes material non-uniformly at the wafer scale as well. An image of a wafer with deposited silicon nitride and silicon oxide layers after the CMP process is shown in Figure 4.3. The color of silicon nitride and silicon oxide on a silicon substrate changes as a function of thickness; the rings formed on the wafer indicate that the thickness of the nitride and oxide layers is non-uniform in the radial direction from the center of the wafer, which has been verified using optical ellipsometry.

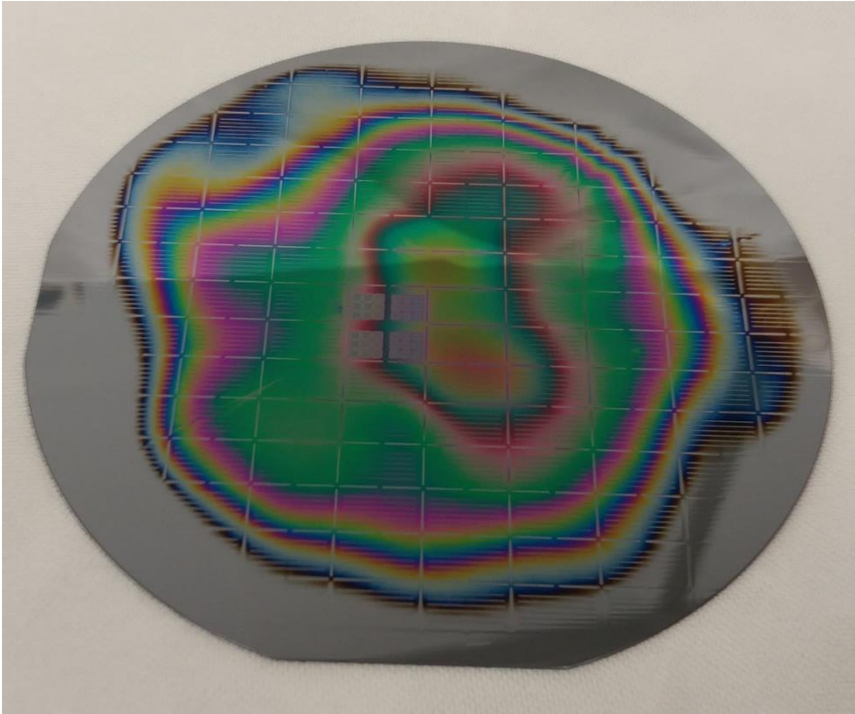

Figure 4.3: Optical image of a 4-inch silicon wafer with deposited silicon nitride and silicon oxide layers after the CMP process. The nitride and oxide layers at the edge of the wafer have been completely removed; the remaining nitride and oxide layers have varying thicknesses, creating color gradients radially from the center of the wafer.

4.3 Conclusion

This chapter presents modifications to the existing sample assembly process for the four-probe thermal measurement devices to create a flat target substrate for sample transfer which will remove most potential sources of contamination. A vertically embedded sacrificial oxide is used to fully support the transferred sample to shield the underside of the graphene from contamination. Vapor etching is then used to suspend the samples instead of wet etching and critical point drying to avoid cross contamination with organic and polymer residues in the critical point dryer.

Chapter 5: Conclusion

Nanostructured materials can exhibit unique size dependent thermal properties because their characteristic dimensions are comparable to the mean free path of heat carriers. Due to their combination of mechanical, electrical, and thermal properties, graphite and its derivatives serve as an excellent platform for studying nanoscale transport phenomena such as hydrodynamic phonon transport. This dissertation presents the development of a nanoscale thermal measurement methodology that is used to measure few-layer graphene and ultrathin graphite. This methodology can also be used for other 2D materials, an active research field.

The thermal properties of few-layer graphene has been measured using the four-probe thermal measurement method, which can measure the intrinsic thermal conductance of a suspended sample as well as isolate the contact thermal resistance between the sample and measurement device. The thermal conductivity of the sample measured was suppressed by polymer residue left from the PMMA carrier film used for sample transfer, preventing the measurement of the true intrinsic properties of the sample and observation of non-diffusive thermal transport.

To prevent direct polymer contact with the thin-film samples, a silicon oxide hard mask was used to shield thin-film samples during transfer. Multiple ultrathin graphite samples were transferred using the shielded hard mask method and measured using the four-probe thermal technique. The thermal conductivities of the ultrathin graphite samples were still below expected values, suggesting other sources of contamination were suppressing thermal performance.

In order to eliminate any remaining sources of sample contamination during sample assembly, a new four-probe thermal measurement device fabrication procedure is presented to prevent polymer contamination on both sides of a thin-film sample. The new

fabrication procedure utilizes a vertically embedded sacrificial oxide that creates a flat target substrate onto which the sample is transferred. The flat substrate also makes the four-probe thermal measurement devices compatible with various polymer-free transfer methods.

The experimental methods presented in this dissertation have laid the groundwork for assembling clean thin-film samples onto the four-probe thermal measurement device so that the true intrinsic thermal properties of thin-film samples can be found. Further efforts utilizing these methods can be used to study the effect of properties such as length and isotope concentration on nanoscale thermal transport. Additionally, these methods can also be used to probe non-diffusive thermal transport in certain materials.

Bibliography

[1] C. Lee, X. Wei, J.W. Kysar, and J. Hone, Science **321**, 385 (2008).
[2] A.K.G. K. S. Novoselov, D.J. S. V. Morozov, and A.A.F. Y. Zhang, S. V. Dubonos, I. V. Grigorieva, Science (80-.). **306**, 666 (2004).
[3] Y. Zhang, Y.-W. Tan, H.L. Stormer, and P. Kim, Nature **438**, 201 (2005).
[4] A. a Balandin, S. Ghosh, W. Bao, I. Calizo, D. Teweldebrhan, F. Miao, and C.N. Lau, Nano Lett. **8**, 902 (2008).
[5] A.L. Moore and L. Shi, Mater. Today **17**, 163 (2014).
[6] P. Goli, S. Legedza, A. Dhar, R. Salgado, J. Renteria, and A.A. Balandin, J. Power Sources **248**, 37 (2014).
[7] M. Zhou, T. Lin, F. Huang, Y. Zhong, Z. Wang, Y. Tang, H. Bi, D. Wan, and J. Lin, Adv. Funct. Mater. **23**, 2263 (2013).
[8] T. Mueller, F. Xia, and P. Avouris, Nat. Photonics **4**, 297 (2010).
[9] P. Avouris, Z. Chen, and V. Perebeinos, Nat. Nanotechnol. **2**, 605 (2007).
[10] J.S. Moon, D. Curtis, S. Bui, T. Marshall, D. Wheeler, I. Valles, S. Kim, E. Wang, X. Weng, and M. Fanton, Electron Device Lett. IEEE **31**, 1193 (2010).
[11] V.P. Gusynin and S.G. Sharapov, Phys. Rev. Lett. **95**, 2 (2005).
[12] M.I. Katsnelson, K.S. Novoselov, and A.K. Geim, Nat. Phys. **2**, 620 (2006).
[13] S. Pisana, M. Lazzeri, C. Casiraghi, K.S. Novoselov, A.K. Geim, A.C. Ferrari, and F. Mauri, Nat. Mater. **6**, 198 (2007).
[14] K.S. Novoselov, a K. Geim, S. V Morozov, D. Jiang, Y. Zhang, S. V Dubonos, I. V Grigorieva, and a a Firsov, Science **306**, 666 (2004).
[15] P. Kim, L. Shi, A. Majumdar, and P.L. McEuen, Phys. Rev. Lett. **87**, 215502 (2001).
[16] G.A. Slack, J. Phys. Chem. Solids **34**, 321 (1973).
[17] L. Lindsay, D.A. Broido, and N. Mingo, Phys. Rev. B **82**, 115427 (2010).
[18] Z. Ding, J. Zhou, B. Song, V. Chiloyan, M. Li, T.-H. Liu, and G. Chen, Nano Lett. **18**, 638 (2018).
[19] S. Lee, D. Broido, K. Esfarjani, and G. Chen, Nat. Commun. **6**, 6290 (2015).
[20] G. Chen, *Nanoscale Energy Transfer and Conversion*, 1st ed. (Oxford University Press, 2005).
[21] S. Lee and L. Lindsay, Phys. Rev. B **95**, 184304 (2017).
[22] S. Ghosh, I. Calizo, D. Teweldebrhan, E.P. Pokatilov, D.L. Nika, a. a. Balandin, W. Bao, F. Miao, and C.N. Lau, Appl. Phys. Lett. **92**, 151911 (2008).
[23] C. Faugeras, B. Faugeras, M. Orlita, M. Potemski, R.R. Nair, and a. K. Geim, ACS Nano **4**, 1889 (2010).
[24] W. Cai, A.L. Moore, Y. Zhu, X. Li, S. Chen, L. Shi, and R.S. Ruoff, Nano Lett. **10**, 1645 (2010).
[25] S. Ghosh, W. Bao, D.L. Nika, S. Subrina, E.P. Pokatilov, C.N. Lau, and A.A. Balandin, Nat. Mater. **9**, 555 (2010).
[26] S. Chen, A.L. Moore, W. Cai, J.W. Suk, J. An, C. Mishra, C. Amos, C.W. Magnuson, J. Kang, L. Shi, and R.S. Ruoff, ACS Nano **5**, 321 (2011).
[27] J.U. Lee, D. Yoon, H. Kim, S.W. Lee, and H. Cheong, Phys. Rev. B - Condens. Matter Mater. Phys. **83**, 1 (2011).

[28] S. Sullivan, A. Vallabhaneni, I. Kholmanov, X. Ruan, J. Murthy, and L. Shi, Nano Lett. **17**, 2049 (2017).
[29] D.G. Cahill, Rev. Sci. Instrum. **73**, 3701 (2002).
[30] M.T. Pettes and L. Shi, Adv. Funct. Mater. **19**, 3918 (2009).
[31] J.H. Seol, I. Jo, A.L. Moore, L. Lindsay, Z.H. Aitken, M.T. Pettes, X. Li, Z. Yao, R. Huang, D. Broido, N. Mingo, R.S. Ruoff, and L. Shi, Science (80-.). **328**, 213 (2010).
[32] W. Jang, W. Bao, L. Jing, C.N. Lau, and C. Dames, Appl. Phys. Lett. **103**, 1 (2013).
[33] M.T. Pettes, I. Jo, Z. Yao, and L. Shi, Nano Lett. **11**, 1195 (2011).
[34] M.M. Sadeghi, I. Jo, and L. Shi, Proc. Natl. Acad. Sci. **110**, 16321 (2013).
[35] J. Wang, L. Zhu, J. Chen, B. Li, and J.T.L. Thong, Adv. Mater. **25**, 6884 (2013).
[36] W. Jang, Z. Chen, W. Bao, C.N. Lau, and C. Dames, Nano Lett. **10**, 3909 (2010).
[37] I. Jo, M.T. Pettes, E. Ou, W. Wu, and L. Shi, Appl. Phys. Lett. **104**, (2014).
[38] I. Jo, M.T. Pettes, L. Lindsay, E. Ou, A. Weathers, A.L. Moore, Z. Yao, and L. Shi, AIP Adv. **5**, 053206 (2015).
[39] J. Kim, E. Ou, D.P. Sellan, and L. Shi, Rev. Sci. Instrum. **86**, 044901 (2015).
[40] B. Smith, B. Vermeersch, J. Carrete, E. Ou, J. Kim, N. Mingo, D. Akinwande, and L. Shi, Adv. Mater. **29**, 1603756 (2017).
[41] E. Ou, X. Li, S. Lee, K. Watanabe, T. Taniguchi, and L. Shi, J. Heat Transfer **141**, 1 (2019).
[42] S.T. Huxtable, D.G. Cahill, and L.M. Phinney, J. Appl. Phys. **95**, 2102 (2004).
[43] Y.S. Touloukian, R.W. Powell, C.Y. Ho, and P.G. Klemens, *Thermophysical Properties of Matter: Thermal Conductivity of Nonmetallic Solids* (IFI/PLENUM, New York-Washington, 1971).
[44] X. Li and S. Lee, Phys. Rev. B **97**, 94309 (2018).
[45] L. Lindsay, D.A. Broido, and N. Mingo, Phys. Rev. B **83**, 235428 (2011).
[46] B. Qiu and X. Ruan, Appl. Phys. Lett. **100**, 193101 (2012).
[47] C. Chen, S. Rosenblatt, K.I. Bolotin, W. Kalb, P. Kim, I. Kymissis, H.L. Stormer, T.F. Heinz, and J. Hone, Nat. Nanotechnol. **4**, 861 (2009).
[48] J. Chan, A. Venugopal, A. Pirkle, S. McDonnell, D. Hinojos, C.W. Magnuson, R.S. Ruoff, L. Colombo, R.M. Wallace, and E.M. Vogel, ACS Nano **6**, 3224 (2012).
[49] A. Pirkle, J. Chan, A. Venugopal, D. Hinojos, C.W. Magnuson, S. McDonnell, L. Colombo, E.M. Vogel, R.S. Ruoff, and R.M. Wallace, Appl. Phys. Lett. **99**, 23 (2011).
[50] K.T. He, J.D. Wood, G.P. Doidge, E. Pop, and J.W. Lyding, Nano Lett. **12**, 2665 (2012).
[51] M. Ishigami, J.H. Chen, W.G. Cullen, M.S. Fuhrer, and E.D. Williams, Nano Lett. **7**, 1643 (2007).
[52] Y. Dan, Y. Lu, N.J. Kybert, Z. Luo, and A.T.C. Johnson, Nano Lett. **9**, 1472 (2009).
[53] P.Y. Huang, C.S. Ruiz-Vargas, A.M. van der Zande, W.S. Whitney, M.P. Levendorf, J.W. Kevek, S. Garg, J.S. Alden, C.J. Hustedt, Y. Zhu, J. Park, P.L. McEuen, and D. a Muller, Nature **469**, 389 (2011).
[54] Y.C. Lin, C.C. Lu, C.H. Yeh, C. Jin, K. Suenaga, and P.W. Chiu, Nano Lett. **12**, 414 (2012).

[55] B. Smith, L. Lindsay, J. Kim, E. Ou, R. Huang, and L. Shi, Appl. Phys. Lett. **114**, 221902 (2019).
[56] T. Kodama, M. Ohnishi, W. Park, T. Shiga, J. Park, T. Shimada, H. Shinohara, J. Shiomi, and K.E. Goodson, Nat. Mater. **16**, 892 (2017).
[57] S.J. Kang, B. Kim, K.S. Kim, Y. Zhao, Z. Chen, G.H. Lee, J. Hone, P. Kim, and C. Nuckolls, Adv. Mater. **23**, 3531 (2011).
[58] X. Li, W. Cai, I.H. Jung, J.H. An, D. Yang, A. Velamakanni, R. Piner, L. Colombo, and R.S. Ruoff, ECS Trans. **19**, 41 (2009).
[59] Y. Lee, S. Bae, H. Jang, S. Jang, S.-E. Zhu, S.H. Sim, Y. Il Song, B.H. Hong, and J.-H. Ahn, Nano Lett. **10**, 490 (2010).
[60] K.S.K.S. Kim, Y. Zhao, H. Jang, S.Y. Lee, J.M. Kim, J.-H. Ahn, P. Kim, J.-Y. Choi, and B.H. Hong, Nature **457**, 706 (2009).
[61] J. Song, F.-Y. Kam, R.-Q. Png, W.-L. Seah, J.-M. Zhuo, G.-K. Lim, P.K.H. Ho, and L.-L. Chua, Nat. Nanotechnol. **8**, 356 (2013).
[62] K. Kim, M. Yankowitz, B. Fallahazad, S. Kang, H.C.P. Movva, S. Huang, S. Larentis, C.M. Corbet, T. Taniguchi, K. Watanabe, S.K. Banerjee, B.J. Leroy, and E. Tutuc, Nano Lett. **16**, 1989 (2016).